Dense Gas and Star Formation in Nearby Infrared-bright Galaxies: APEX Survey of HCN and HCO+ J=2 -> 1

The Astrophysical Journal, 936:58 (23pp), 2022 September 1 https://doi.org/10.3847/1538-4357/ac82eb

Dense Gas and Star Formation in Nearby Infrared-bright Galaxies: APEX Survey of HCN and HCO^+ $J = 2 \rightarrow 1$

Jing Zhou[1,2], Zhi-Yu Zhang[1,2], Yu Gao[3,4], Junzhi Wang[5,6], Yong Shi[1,2], Qiusheng Gu[1,2], Chentao Yang[7,8], Tao Wang[1,2], and Qing-Hua Tan[4]

[1] School of Astronomy and Space Science, Nanjing University, Nanjing 210093, People's Republic of China; zzhang@nju.edu.cn
[2] Key Laboratory of Modern Astronomy and Astrophysics (Nanjing University), Ministry of Education, Nanjing 210093, People's Republic of China
[3] Department of Astronomy, Xiamen University, Xiamen, Fujian 361005, People's Republic of China
[4] Purple Mountain Observation & Key Laboratory for Radio Astronomy, Chinese Academy of Science, 10 Yuanhua Road, Nanjing 210033, People's Republic of China
[5] Shanghai Astronomical Observatory, Chinese Academy of Science, 80 Nandan Road, Shanghai 200030, People's Republic of China
[6] Department of Physics, Guangxi University, Nanning 530004, People's Republic of China
[7] Department of Space, Earth and Environment, Chalmers University of Technology, Onsala Space Observatory, SE-439 92 Onsala, Sweden
[8] European Southern Observatory, Alonso de Córdova 3107, Vitacura, Casilla 19001, Santiago de Chile, Chile
Received 2021 September 20; revised 2022 July 19; accepted 2022 July 19; published 2022 August 30

Abstract

Both Galactic and extragalactic studies of star formation suggest that stars form directly from dense molecular gas. To trace such high volume density gas, HCN and HCO^+ $J = 1 \rightarrow 0$ have been widely used for their high dipole moments, relatively high abundances, and often being the strongest lines after CO. However, HCN and HCO^+ $J = 1 \rightarrow 0$ emission could arguably be dominated by the gas components at low volume densities. The HCN $J = 2 \rightarrow 1$ and HCO^+ $J = 2 \rightarrow 1$ transitions, with more suitable critical densities (1.6×10^6 and 2.8×10^5 cm^{-3}) and excitation requirements, would trace typical dense gas closely related to star formation. Here we report new observations of HCN $J = 2 \rightarrow 1$ and HCO^+ $J = 2 \rightarrow 1$ toward 17 nearby infrared-bright galaxies with the APEX 12 m telescope. The correlation slopes between the luminosities of HCN $J = 2 \rightarrow 1$ and HCO^+ $J = 2 \rightarrow 1$ and total infrared emission are 1.03 ± 0.05 and 1.00 ± 0.05, respectively. The correlations of their surface densities, normalized with the area of radio/submillimeter continuum, show even tighter relations (slopes: 0.99 ± 0.03 and 1.02 ± 0.03). The eight active galactic nucleus (AGN)–dominated galaxies show no significant difference from the 11 star-formation–dominated galaxies in the above relations. The average HCN/HCO^+ ratios are 1.15 ± 0.26 and 0.98 ± 0.42 for AGN- and star-formation–dominated galaxies, respectively, without obvious dependencies on infrared luminosity, dust temperature, or infrared pumping. The Magellanic Clouds roughly follow the same correlations, expanding to 8 orders of magnitude. On the other hand, ultraluminous infrared galaxies with AGNs systematically lie above the correlations, indicating potential biases introduced by AGNs.

Unified Astronomy Thesaurus concepts: Star formation (1569); Starburst galaxies (1570); Dense interstellar clouds (371); Dust continuum emission (412); Interstellar molecules (849)

1. Introduction

Stars, as building blocks of galaxies, contribute most of the radiation of galaxies, dominate the metal enrichment of galaxies, drive galactic outflows, and essentially construct galaxy structures. Therefore, star formation (SF) activity is one of the most important evolutionary processes in galaxies (Kennicutt & Evans 2012). It has been found that molecular gas supplies the raw material of SF, while the majority of molecular gas is not directly observable from the H_2 emission (Bolatto et al. 2013). Molecular gas is often traced with the rotational transitions of other molecules excited by collisions with H_2 molecules. Among them, CO transitions mostly trace the bulk of molecular gas due to its weak permanent dipole moment ($\mu_{10}^e = 0.11$ D; Solomon & Vanden Bout 2005) and low upper energy levels (5.5 K for $J = 1 \rightarrow 0$; Schöier et al. 2005), while the dense gas tracers, e.g., rotational transitions of HCN, HCO^+, CS, N_2H^+, etc., can trace denser molecular clouds due to their much higher dipole moments ($\mu_{10}^e =$ 2.98 and 3.92 D for HCN and HCO^+ $J = 1 \rightarrow 0$, respectively; Papadopoulos 2007).

The SF rates (SFRs) in galaxies, on the other hand, are usually traced with ultraviolet continuum emission, optical line tracers such as Hα and [O II], dust emission at infrared (IR) wavelengths, radio continuum emission, or X-ray emission (Kennicutt 1998a; Kennicutt & Evans 2012). Among them, the IR emission from dust normally traces the bolometric energy heated up by the young stars. The IR emission is generally extinction-free and often covered by multi-IR-wavelength space telescopes such as Herschel (Pilbratt et al. 2010), Spitzer (Werner et al. 2004), the Infrared Astronomical Satellite (IRAS; Neugebauer et al. 1984), etc. Therefore, the total IR luminosity is widely adopted as an SFR tracer for gas-rich galaxies (e.g., Galametz et al. 2016, 2020).

A long-standing question remains: which gas is forming stars? Kennicutt (1998b) found a superlinear correlation between the surface densities of SFR and total gas mass, where the area was defined by CO $J = 1 \rightarrow 0$ or IR images. This correlation, however, turns to a linear shape with a slope index of unity when the sample is limited to nearby normal spiral galaxies beyond 500 pc scales (e.g., Bigiel et al. 2008). On the other hand, Gao & Solomon (2004a) found that the dense molecular gas traced by HCN $J = 1 \rightarrow 0$ is the direct source of SF. This correlation is further connected to Galactic massive star-forming regions on subparsec scales (Wu et al. 2005, 2010). Furthermore,

Heiderman et al. (2010) also found a similar result by counting young stellar objects in Galactic dense molecular clouds.

However, the emission of HCN $J=1\rightarrow0$ and HCO^+ $J=1\rightarrow0$ could be largely contaminated by diffuse gas with relatively high column densities (Evans et al. 2020). Although the high-J transitions (e.g., $J=3\rightarrow2$ and $J=4\rightarrow3$) of HCN and HCO^+ (Zhang et al. 2014; Tan et al. 2018; Li et al. 2020b) are found to have linear correlations with SFR, these high-J transitions are mainly from the densest molecular cores heated by massive stars and leave out most emission from cold clumps.

The HCN $J=2\rightarrow1$ and HCO^+ $J=2\rightarrow1$, which have moderate critical densities ($n_{\rm crit}^{\rm HCN2-1}=\sim1.6\times10^6$ and $n_{\rm crit}^{\rm HCO^+\,2-1}=\sim2.8\times10^5\,{\rm cm^{-3}}$ for conditions of a kinetic temperature $T_{\rm kin}\sim50$ K, optically thin, and no background; Shirley 2015) and suitable upper energy levels ($E_{\rm up}^{\rm HCN2-1}=12.76$ and $E_{\rm up}^{\rm HCO^+\,2-1}=12.84$K, respectively; Shirley 2015), could avoid the aforementioned disadvantages of other transitions. On the other hand, the rest frequency of HCN $J=2\rightarrow1$ is close to the H_2O 177.3 GHz line in the Earth's atmosphere, so the observation needs excellent weather conditions for nearby galaxies.

In this paper, we present Atacama Pathfinder Experiment (APEX) observations of HCN $J=2\rightarrow1$ and HCO^+ $J=2\rightarrow1$ in a sample of 17 IR-bright galaxies. In Section 2, we describe observations with the APEX 12 m telescope and the ancillary data adopted in this paper. In Section 3, we describe methods to derive line luminosities, photometry, and dust properties. In Section 4, we present the obtained spectra, correlations between SFR and dense gas tracers, and line ratios. In Section 5, we discuss the assumptions, caveats, and physical implications of our results. In Section 6, we summarize our work. We adopt cosmological parameters of $H_0=71\,{\rm km\,s^{-1}\,Mpc^{-1}}$, $\Omega_{\rm M}=0.27$, and $\Omega_\Lambda=0.73$ throughout this work (Spergel et al. 2007).

2. Observation and Data Reduction

2.1. Sample Selection

Our sample was selected from the survey of CS $J=7\rightarrow6$, HCN $J=4\rightarrow3$, and HCO^+ $J=4\rightarrow3$ (Zhang et al. 2014), which contains nearby normal galaxies and luminous and ultraluminous IR galaxies (ULIRGs). These galaxies were originally selected from the IRAS Revised Bright Galaxy Sample (Sanders et al. 2003). All galaxies have $S_\nu(100\,\mu{\rm m})>100$ Jy and decl. $<20^\circ$ to be accessible from APEX. We exclude three targets without any detection of HCN $J=4\rightarrow3$ and HCO^+ $J=4\rightarrow3$. The final sample consists of 19 galaxies, which include 17 newly observed galaxies and two ULIRGs from the literature, Arp 220 (Galametz et al. 2016) and Superantennae (Imanishi et al. 2022).

The total IR luminosities range from 1.8×10^{10} to 1.8×10^{12} $L_\odot$, which implies a range of SFR from 3.6 to $360\,M_\odot\,{\rm yr^{-1}}$. The distance range is ~3.72–273 Mpc. The molecular gas masses (estimated from CO $J=1\rightarrow0$) range from 4×10^8 to $2.1\times10^{10}\,M_\odot$. We further divide the sample into active galactic nucleus (AGN)–dominated and SF-dominated galaxies according to the classifications of the NASA/IPAC Extragalactic Database (NED).[9] The final sample consists of eight AGN-dominated and 11 SF-dominated galaxies. The basic information of the sample is shown in Table 1.

2.2. HCN J = 2 → 1 and HCO^+ J = 2 → 1 Observations

The observation was conducted with the APEX 12 m telescope during 2016 July and August (project ID: E-097.B-0986A-2016). The weather conditions were good (precipitable water vapor, PWV, <0.9 mm) for 10 sources and normal (PWV ~ 1–1.4 mm) for the rest. The wobbler switching mode was adopted for all observations with a switching frequency of 2 Hz and a beam throw of 120″ at each side of the target. The beam size was ~34.″7 (from 34.″2 to 35.″2), on average, with a slight variation between targets, depending on the specific line and redshift.

We employed the Swedish-ESO PI Instrument for APEX (SEPIA) receivers (Belitsky et al. 2018) to simultaneously observe HCN $J=2\rightarrow1$ and HCO^+ $J=2\rightarrow1$, which have rest frequencies of 177.261 and 178.375 GHz, respectively. The SEPIA-180 receiver offers two sidebands, double polarizations, and a 4 GHz bandwidth for each sideband. The two targeted lines are configured in the lower sideband. Focusing calibrations were conducted on Mars, Jupiter, IRAS 15194–5115, IK Tau, and R Dor every 3–4 hr. Pointing calibrations were conducted on Mars, Jupiter, or nearby (<10°) carbon stars every hour.

We used the CLASS package in GILDAS[10] to reduce the spectral line data. We checked the quality of all spectra by eye, fitted the baseline with a first-order polynomial profile, and averaged them together. Each sideband has 104,851 channels with an initial velocity resolution of 0.0644 $\rm km\,s^{-1}$. We smoothed each spectrum to a velocity resolution of 26 $\rm km\,s^{-1}$, at which the final rms noise ranges from 1.5 to 2 mK. The main beam temperature, $T_{\rm mb}$, is converted from the antenna temperature, $T_{\rm A}^*$, using $T_{\rm mb}=T_{\rm A}^*\eta_{\rm f}/\eta_{\rm mb}$, where $\eta_{\rm f}=0.95$ is the forward efficiency, and $\eta_{\rm mb}=0.73$ is the main beam efficiency. We adopt the kelvin-to-jansky conversion factor 39 Jy/K to convert $T_{\rm A}^*$ to flux density from the beam-covered regions. The observational results are shown in Table 2, including integrated flux, Gaussian fitting FWHM velocity width, and Gaussian fitting peak flux density.

2.3. IR Data

We obtained multiwavelength photometric data of the Photodetector Array Camera and Spectrometer (PACS; for 70, 100, and 160 μm; Poglitsch et al. 2010) and the Spectral and Photometric Imaging REceiver (SPIRE; for 250, 350, and 500 μm; Griffin et al. 2010) on board the Herschel Space Observatory. These data were processed to level 2.5 and downloaded from the European Space Agency.[11] We also downloaded the available 24 μm data from the archival Spitzer Space Telescope (Rieke et al. 2004), which were processed to level 2. The beam sizes in half-power beamwidth (HPBW) are 13.″9, 6.″4, 5.″7, 7″, 11.″2, 18.″2, 24.″9, and 36.″1 for Wide-field Infrared Survey Explorer (WISE) 22 μm; Multiband Imaging Photometer for Spitzer (MIPS) 24 μm; PACS 70, 100, and 160 μm; and SPIRE 250, 350, and 500 μm, respectively.

Because some nearby galaxies cannot be fully enclosed by the APEX beam, we further measured the emission size of the PACS 70 μm images with the diameter that encloses 90% of the

[9] http://ned.ipac.caltech.edu/

[10] https://www.iram.fr/IRAMFR/GILDAS/

[11] http://archives.esac.esa.int/hsa/whsa/

Table 1
Basic Information

Source Name	R.A. (h,m,s)	Decl. (d,m,s)	Redshift (z)	Distance[a] (Mpc)	Reference	HPBW$^{1.4\ GHz}$ (arcsec)	Reference	$S_{VLA}^{1.4GHz}$[d] (mJy)	$S_{VLBI}^{1.4GHz}$ (mJy)	$S_{COJ=1-0}$ (Jy km s^{-1})	Type
NGC 4945	13:05:27.51	−49:28:06.0	0.00188	3.8 ± 0.3	1	7.9 × 4.3	9	6450	33	9887 ± 28	AGN
NGC 1068	02:42:40.70	−00:00:48.0	0.00379	10.1 ± 2.0	1	9.2 × 2.2	9	4848	2.6	1903 ± 77	AGN
NGC 7552	23:16:10.70	−42:35:05.0	0.00536	14.8 ± 1.3	2	7.3 × 7.1	9	280	...[e]	652 ± 88	SF
NGC 4418	12:26:54.61	−00:52:39.0	0.00727	23.9 ± 2.2	3	0.5	10	41	...[e]	132 ± 28	SF
NGC 1365	03:33:36.40	−36:08:25.0	0.00546	17.5 ± 3.5	1	21.7 × 10.5	9	376	4.57[f]	2166 ± 102	AGN
NGC 3256	10:27:51.30	−43:54:13.0	0.00935	37.4 ± 6.0	4	12.2 × 9.3	9	668	...[e]	1223 ± 8	SF
NGC 1808	05:07:42.30	−37:30:47.0	0.00332	12.3 ± 2.5	1	14 × 8.8	9	528	...[e]	1898 ± 137	SF
IRAS 13120–5453	13:15:06.30	−55:09:23.0	0.031249	129.3 ± 9.1	1	1.5 × 0.5	9	118	...[e]	126 ± 13	SF
IRAS 13242–5713	13:27:23.80	−57:29:22.0	0.009788	37.6 ± 2.6	5	6 × 3.7	9	97	...[e]	...	SF
Mrk 331	23:51:26.80	+20:35:10.0	0.01848	53 ± 5	3	2.53	11	71	<7.5	49.5 ± 3.7	SF
NGC 6240A	16:52:58.90	+02:24:03.5	0.02488	103 ± 7	6	0.66 × 0.42	12[b]	396	5.4	333.2 ± 33	AGN
NGC 6240B	16:52:58.91	+02:24:04.2				1.03 × 0.41					
NGC 3628	11:20:17.00	+13:35:23.0	0.00281	10.3 ± 0.4	7	71	13	476	<4.5	1309 ± 25	SF
NGC 3627	11:20:14.90	+12:59:30.0	0.00243	10.7 ± 0.5	1	160	13	459	<3.39	4477 ± 75	AGN
IRAS 18293–3413	18:32:41.10	−34:11:27.0	0.017996	74.8 ± 5.3	5	5.9 × 4.9	9	226	...[e]	686.1 ± 7.6	SF
NGC 7469	23:03:15.60	−08:52:26.0	0.01632	59.7 ± 1.6	3	3.3	11	181	32.5	48.1 ± 3.5	AGN
IRAS 17578–0400	18:00:31.90	−04:00:53.0	0.013325	60 ± 6	3	3 × 2.3	9	80	...[e]	...	SF
IC 1623	01:07:47.20	−17:30:25.0	0.02007	80.9 ± 5.7	6	15	11	249	4.7	291 ± 45	AGN
Arp 220A	15:34:57.29	+23:30:11.3	0.01813	84.1 ± 5.9	6	0.27 × 0.24	12[c]	515	91.25	515 ± 51	SF
Arp 220B	15:34:57.22	+23:30:11.5				0.49 × 0.31					
IRAS 19254–7245	19:31:21.40	−72:39:18.0	0.06171	273 ± 18	8	0.5	14	...	...	58.8 ± 5.9	AGN

Notes.
[a] We adopt redshift-independent distances measures with the Tully–Fisher relation, tip of the red giant branch stars, Type Ia supernovae, and Cepheids from NED for most of the galaxies. Objects NGC 1068, NGC 7552, NGC 4418, NGC 3265, NGC 1808, Mrk 331, NGC 3628, and IRAS 17578–0400 are measured using the Tully–Fisher relation (Tully & Fisher 1988; Russell 2002; Theureau et al. 2007; Nasonova et al. 2011; Tully et al. 2013). Objects NGC 4945 and NGC 3627 are measured with tip of the red giant branch stars (Tully et al. 2015; Jang & Lee 2017). Object NGC 1365 is measured with Cepheids (Willick & Batra 2001). Object NGC 7469 is measured with Type Ia supernovae (Koshida et al. 2017). We adopt the Hubble flow distance of the rest of the galaxies in our sample (de Vaucouleurs et al. 1991; Karachentsev & Makarov 1996; Mould et al. 2000).
[b] The size of NGC 6240 is estimated from two-component Gaussian fitting of the ALMA 480 GHz continuum observation (project code: 2015.1.00717.S).
[c] The measurement of Arp 220 uses a combination of data from the VLA A-configuration and MERLIN from Varenius et al. (2016).
[d] The fluxes of the 1.4 GHz continuum only have the uniform error of the survey, and the errors of individual galaxies are hard to determine.
[e] These galaxies are all SF-dominated, so their supermassive black holes would not affect the 1.4 GHz continuum size (Saikia et al. 1990; Varenius et al. 2014; Herrero-Illana et al. 2017).
[f] The high-resolution 1.4 GHz flux of NGC 1365 comes from the VLA observation in Sandqvist et al. (1995).
References. (1) Nasonova et al. (2011); (2) Russell (2002); (3) Theureau et al. (2007); (4) Tully & Fisher (1988); (5) de Vaucouleurs et al. (1991); (6) Mould et al. (2000); (7) Tully et al. (2013); (8) Fixsen et al. (1996); (9) Condon et al. (2021); (10) Costagliola et al. (2013); (11) Liu et al. (2015); (12) this work; (13) Condon (1987); (14) Imanishi et al. (2016).

Table 2
Observational Result

Source Name	HCN $J = 2 \rightarrow 1$			HCO^+ $J = 2 \rightarrow 1$			$Diameter_{70}$[a]
	Integrated Flux (Jy km s^{-1})	FWHM (km s^{-1})	Peak (mJy)	Integrated Flux (Jy km s^{-1})	FWHM (km s^{-1})	Peak (mJy)	(arcsec)
NGC 4945	885 ± 11	328.2 ± 1.9	3120 ± 27	855 ± 11	328.1 ± 2.7	2917 ± 35	85.2[b]
NGC 1068	243.5 ± 6.4	257.9 ± 6.3	1076 ± 35	180 ± 6	253.4 ± 8.7	807 ± 39	38.6[b]
NGC 7552	63.7 ± 6.0	138.5 ± 8.6	546 ± 47	85.8 ± 5.9	166.7 ± 11.1	593 ± 55	21.9[c]
NGC 4418	54.4 ± 5.9	193 ± 20	261 ± 35	38.7 ± 5.9	107 ± 17	215 ± 43	11.3
NGC 1365	95.7 ± 8.7	328 ± 29	343 ± 39	71.1 ± 8.5	241 ± 24	351 ± 47	19.2[c]
NGC 3256	57.9 ± 7.6	180 ± 18	398 ± 55	106.1 ± 7.6	181 ± 11	683 ± 59	19.5
NGC 1808	55.7 ± 7.5	236 ± 25	289 ± 43	58.0 ± 7.4	156 ± 29	394 ± 90	22.9[c]
IRAS 13120–5453	48 ± 11	333 ± 52	187 ± 39	43 ± 11	362 ± 85	152 ± 47	11.5
IRAS 13242–5713	57 ± 11	223 ± 42	300 ± 78	108 ± 11	194 ± 18	636 ± 82	16.7
Mrk 331	30.4 ± 8.3	214 ± 83	101 ± 27	<32	...	...	11.0
NGC 6240	61 ± 15	809 ± 142	101 ± 23	83 ± 15	640 ± 84	152 ± 27	11.4
NGC 3628	41 ± 11	235 ± 58	187 ± 59	55 ± 11	210 ± 30	289 ± 59	42.5[b]
NGC 3627	46 ± 12	332 ± 62	179 ± 43	<54	...	...	63.8[b]
IRAS 18293–3413	35 ± 10	332 ± 105	117 ± 51	60 ± 10	418 ± 96	164 ± 47	12.3
NGC 7469	<50.2	...	...	39.8 ± 9.9	287 ± 61	164 ± 47	11.7
IRAS 17578–0400	<38.2	...	...	<33	...	...	11.7
IC 1623	<32.1	...	...	30.6 ± 8.8	208 ± 47	187 ± 55	14.0

Notes.
[a] Diameter of the PACS 70 μm image that encloses 90% of the flux of the entire galaxy, which is convolved with the PACS 70 μm 5.″7 beam.
[b] Objects NGC 4945, NGC 1068, NGC 3628, and NGC 3627 have larger diameters than the APEX beam.
[c] Objects NGC 7552, NGC 1365, and NGC 1808 have long-structure disks that cannot be enclosed by the APEX beam.

flux of the entire galaxy and listed them in Table 2. From the PACS 70 μm images, seven galaxies (NGC 4945, NGC 1068, NGC 7552, NGC 1365, NGC 1808, NGC 3627, and NGC 3628) have sizes (in diameter) larger than the APEX beam or cannot be fully covered by the APEX beam, while the other 12 galaxies are fully enclosed by the APEX beam of 34.″7 (FWHM). For these 12 pointlike galaxies, we adopt the 25, 60, and 100 μm fluxes from the RBGS survey (Sanders et al. 2003), which was obtained with angular resolutions of 0.′7, 1.′7, and ∼3′, respectively. For the seven extended galaxies, we adopt IRAS fluxes scaled from other wavelengths, as described in Section 3.2.

2.4. Radio Continuum

We assume that the 1.4 GHz radio continuum emission is dominated by synchrotron radiation from supernova remnants (White 1985) and free–free radiation from H II regions (Condon & Ransom 2016); both would trace recent star-forming activities. We use the 1.4 GHz radio continuum to measure the size of the star-forming region, assuming that SF contributes the majority of the radio flux. To verify this assumption and check for possible AGN contamination, very high resolution radio data are needed. Therefore, we collected very long baseline interferometric (VLBI) data in the literature, which are only available for a few targets.

For galaxies with multiple measurements of the radio size, we adopt the ones observed with the highest angular resolutions (Table 1). Ten galaxies have sizes measured from MeerKAT data, which have an angular resolution of ∼7.″5 (Condon et al. 2021). The sizes of NGC 3627 and NGC 3628 were measured using the NRAO VLA Sky Survey (Condon 1987), which has an angular resolution of 45″. The size of NGC 4418 is estimated from MERLIN observations at a resolution of 0.″35 × 0.″16 (Costagliola et al. 2013). We adopt the 250 GHz Atacama Large Millimeter/submillimeter Array (ALMA) continuum size for IRAS 19254–7245, which was measured by Imanishi et al. (2016).

For other galaxies, we measured their sizes using data downloaded from the ALMA data archive and the literature. We fit the maps with a 2D Gaussian profile using the task IMFIT in CASA (McMullin et al. 2007). The 1.4 GHz continuum data of Arp 220 were combined with MERLIN and VLA A-configuration data in the literature (Varenius et al. 2016). Objects NGC 6240 and IRAS 19254–7245 have strong AGN contributions to the 1.4 GHz continuum; we estimate their sizes using ALMA dust continuum data. We download the ALMA 480 GHz data of NGC 6240 (project code: 2015.1.00717.S) and fit its sizes with a two-component Gaussian model (NGC 6140A and NGC 6240B in Table 1).

The sizes and fluxes of the radio continuum are from the whole galaxies. When computing luminosity surface densities in Section 4.3, we adopt the radio area for galaxies with radio sizes smaller than the APEX beam. For galaxies with radio sizes larger than the APEX beam, we adopt the APEX beam area to compute the surface densities.

2.5. Ancillary CO Data

Most of the velocity-integrated CO $J = 1 \rightarrow 0$ fluxes come from Baan et al. (2008), observed with the Institut de Radioastronomie Millimetrique (IRAM) 30 m telescope (HPBW ∼ 21″) and the Swedish-ESO Submillimeter Telescope 15 m telescope (HPBW ∼ 45″). The CO fluxes of IRAS 13120–5453 and NGC 4418 are from Sliwa et al. (2017) and Papadopoulos et al. (2012) observed with ALMA and the IRAM 30 m, respectively. However, there are no low-J CO data available for IRAS 13242–5713 and IRAS 17578–0400.

3. Method and Analysis

3.1. HCN and HCO^+ J = 2 → 1 Line Luminosity

We calculate the velocity-integrated main beam temperature and associated thermal noise following Greve et al. (2009),

$$\sigma\left(\int_{\Delta_v} T_{\rm mb} dv\right) = \sqrt{N_{\Delta_v}}\left(1 + \frac{N_{\Delta_v}}{N_{\rm bas}}\right)^{1/2} \times \sigma(T_{\rm mb,ch})\Delta v_{\rm ch} + 10\% \int_{\Delta_v} T_{\rm mb} dv, \quad (1)$$

where $v_{\rm ch} = 26$ km s^{-1} is the final velocity resolution, $N_{\Delta_v} = (\Delta v/\Delta v_{\rm ch})$ is the number of channels that cover the line, $N_{\rm bas}$ is the number of line-free channels, and $\sigma(T_{\rm mb,ch})$ is the channel-to-channel rms noise. We adopt 10% as the absolute flux calibration error during observation.

Then we computed the line luminosities of the region observed in the whole galaxy using the equation from Gao & Solomon (2004b),

$$L' = \pi/(4\ln 2)\theta_{\rm mb}^2 \int_{\Delta_v} T_{\rm mb} dv\, D_{\rm L}^2 (1+z)^{-3}, \quad (2)$$

where the luminosity distance, $D_{\rm L}$, and redshift, z, are taken from NED (Table 1). We further propagate the uncertainties from the distance and flux to the final error of the line luminosities using the following formula:

$$\sigma_{\rm flux}(L') = \pi/(4\ln 2)\theta_{\rm mb}^2 \times (1+z)^{-3} D_{\rm L}^2\, \sigma\left(\int_{\Delta_v} T_{\rm mb} dv\right), \quad (3)$$

$$\sigma_{\rm dist}(L') = \pi/(4\ln 2)\theta_{\rm mb}^2 (1+z)^{-3} \times 2D_{\rm L} \times \int_{\Delta_v} T_{\rm mb} dv\, \sigma(D_{\rm L}), \quad (4)$$

$$\sigma(L') = \sqrt{\sigma_{\rm flux}^2(L') + \sigma_{\rm dist}^2(L')}, \quad (5)$$

where $\sigma_{\rm flux}(L')$ is the luminosity error propagated from the flux error, $\sigma_{\rm dist}(L')$ is the luminosity error propagated from the distance estimation, and $\sigma(D_{\rm L})$ is the distance error. Because all luminosities adopt the same distance, their ratios do not include errors of distances.

3.2. Photometry, IR Luminosity, and Dust Temperature

Because our APEX observations have different beam sizes compared to that of the IR photometric data, it is not possible to directly compare dense gas tracers with IR data. Therefore, we convolve the Spitzer and Herschel maps to match the beam size of the APEX 12 m data, a 34.″7 (diameter) Gaussian beam, using the convolution kernels provided by Aniano et al. (2011). Compared to aperture photometry, this method is more robust and much less affected by the spatial distribution of the target (e.g., Tan et al. 2018). Details of the method were described in Tan et al. (2018).

To measure the photometric flux at each wavelength and estimate the associated noise levels, our photometry procedures are as follows. First, we subtract the background of an annulus region from 1.5× to 2× the maximum source size, which is estimated using the curve of growth (see Appendix A for details). Second, we scale the image units to janskys per beam by a factor of $\pi/4\ln 2 \times ({\rm HPBW_{beam}/pixelsize})^2$. Third, we measure the value of the central pixel to obtain the flux density at each IR band. Last, the error is estimated from the background regions. The photometric results are listed in Table 3. The flux error consists of photometric, flux calibration, and systematic errors. We adopt an absolute flux calibration error of 7% and a systematic error of 3% following Balog et al. (2014).

Since the IRAS and Herschel SPIRE 500 μm data have lower resolutions than our APEX data, we scale the IRAS 25 and 60 μm and SPIRE 500 μm data to obtain the beam-matched fluxes using aperture correction factors obtained from MIPS 24 μm, PACS 70 μm, and SPIRE 350 μm maps, respectively. For example, we measure the flux of the entire galaxy ($S_{70}^{\rm total}$) and in the 34.″7 Gaussian beam of the PACS 70 μm ($S_{70}^{\rm beam}$). Then we adopt $S_{60}^{\rm total} * S_{70}^{\rm beam}/S_{70}^{\rm total}$ as the IRAS 60 μm flux in the beam.

We then build a dust spectral energy distribution (SED) for each galaxy and fit the total IR luminosity and dust temperature. We fit the data with a two-component modified blackbody (MBB) dust model following Galametz et al. (2013). Since the warm dust component contributes a nonnegligible fraction to the 70 and 100 μm emission, a single MBB model would not match the Wien side of the SED and would overestimate the cold dust component. The two-component MBB model is described as follows:

$$S_\nu = A_{\rm w}\, \lambda^{-2} B_\nu(T_{\rm w}) + A_{\rm c}\, \lambda^{-\beta_{\rm c}} B_\nu(T_{\rm c}), \quad (6)$$

where S_ν is the flux density obtained from photometry; B_ν is the Planck function; $\beta_{\rm c}$ is the emissivity index of the cold component; $T_{\rm w}$ and $T_{\rm c}$ are the temperature of the warm and cold components, respectively; and $A_{\rm c}$ and $A_{\rm w}$ describe the peaks of the two components, respectively. To limit the number of free parameters, we fix $\beta_{\rm w} = 2.0$ as a good approximation of the dust model of Li & Draine (2001). So, the estimate of $T_{\rm w}$ has an additional systematic error compared to $T_{\rm c}$.

We fit the SEDs and estimate the uncertainties using the Markov Chain Monte Carlo (MCMC) package EMCEE (Foreman-Mackey et al. 2013). Details of the dust SED fitting are shown in Appendix B. Parameters obtained from the SED fitting are listed in Table 4. Then we compute the total IR luminosity by integrating from 3 to 1000 μm as $L_{\rm IR}$, which is adopted as the SFR tracer. The beam-matched $L_{\rm IR}$ accounts for ∼10%–100% of $L_{\rm IR}^{\rm whole}$ from the whole galaxy provided by Sanders et al. (2003). In Appendix C, we present $L'_{\rm HCN}$–$L_{\rm IR}$ correlations between far-IR luminosity (from 100 to 1000 μm), near-to-mid-IR luminosity (from 3 to 100 μm), and IR luminosity of the warm dust component.

The $L_{\rm IR}$ within the 34.″7 beam area ranges from 2.7×10^9 to $1.7 \times 10^{12}\, L_\odot$. The cold dust temperature $T_{\rm c}$ ranges from 16.9 to 32.3 K, with an average value of 24 K. Compared with the result of the overlapped galaxies in U et al. (2012), our dust temperature is lower, possibly because of the inclusion of the Herschel/SPIRE data, which would better constrain the cold dust component. Our fitting result is consistent with Galametz et al. (2013).

3.3. Molecular Gas Mass and SFR Estimation

In this work, we derive the dense gas mass from $L'_{\rm HCNJ=2\to1}$ and $L'_{\rm HCO^+J=2\to1}$ following Gao & Solomon (2004b):

$$M_{\rm dense}({\rm H_2}) \approx 2.1 \frac{\langle n({\rm H_2})\rangle^{1/2}}{T_{\rm b}} L'_{\rm HCN\ 1-0} \sim 10\, L'_{\rm HCN\ 1-0}\, M_\odot ({\rm K\ km\ s^{-1}\ pc^2})^{-1}, \quad (7)$$

where $\langle n({\rm H_2})\rangle$ is the average density of the dense gas, and $T_{\rm b}$ is the brightness temperature of the dense gas tracer. The

Table 3
IR Fluxes Inside the APEX Beam

Source Name	MIPS 24 (Jy beam^{-1})	IRAS 25 (Jy)	IRAS 60 (Jy)	PACS 70 (Jy beam^{-1})	PACS 100 (Jy beam^{-1})	PACS 160 (Jy beam^{-1})	SPIRE 250 (Jy beam^{-1})	SPIRE 350 (Jy beam^{-1})	SPIRE 500 (Jy beam^{-1})
NGC 4945	9.7 ± 1.0	42.3 ± 4.3	625.5 ± 62.7	734.5 ± 73.5	1060 ± 106	883.8 ± 88.4	333 ± 33	124 ± 12	33.1 ± 3.3
NGC 1068	31.4 ± 3.2	87.6 ± 8.9	196.4 ± 19.7	180.7 ± 18.1	...	146.4 ± 14.7	51.1 ± 5.1	18.3 ± 1.8	5.0 ± 0.51
NGC 7552	...	11.9 ± 1.2	77.4 ± 7.8	82.5 ± 8.3	95.6 ± 9.6	67.1 ± 6.9	22.5 ± 2.3	7.6 ± 0.8	2.0 ± 0.21
NGC 4418	5.9 ± 0.7	9.7 ± 1.1	43.9 ± 4.5	41.5 ± 4.2	33.0 ± 3.3	18.1 ± 1.8	6.2 ± 0.6	2.3 ± 0.2	0.7 ± 0.08
NGC 1365	8.2 ± 0.8	14.3 ± 1.5	94.3 ± 9.5	95.7 ± 9.6	132.4 ± 13.3	111.4 ± 11.2	46.5 ± 4.7	17.8 ± 1.8	5.1 ± 0.52
NGC 3256	11.1 ± 1.1	15.7 ± 1.6	102.6 ± 10.3	111.3 ± 11.1	120.7 ± 12.1	82.5 ± 8.3	26.9 ± 2.7	8.7 ± 0.9	2.5 ± 0.26
NGC 1808	9.7 ± 1.0	17.0 ± 1.7	105.5 ± 10.6	113.1 ± 11.3	130.5 ± 13.1	94.7 ± 9.5	33.6 ± 3.4	11.6 ± 1.2	3.1 ± 0.32
IRAS 13120–5453	2.4 ± 0.2	3.0 ± 0.3	41.1 ± 4.2	47.7 ± 4.8	52.3 ± 5.2	33.7 ± 3.4	11.7 ± 1.2	4.1 ± 0.4	1.0 ± 0.12
IRAS 13242–5713	5.5 ± 0.6	7.6 ± 0.8	81.4 ± 8.2	91.5 ± 9.2	98.1 ± 9.8	66.0 ± 6.7	23.0 ± 2.4	7.9 ± 0.9	2.2 ± 0.25
Mrk 331	1.9 ± 0.2	2.5 ± 0.3	18.0 ± 1.8	20.0 ± 2.0	22.5 ± 2.3	16.3 ± 1.7	5.8 ± 0.6	2.1 ± 0.2	0.5 ± 0.06
NGC 6240	2.9 ± 0.3	3.5 ± 0.4	22.9 ± 2.3	25.0 ± 2.5	26.2 ± 2.6	17.2 ± 1.9	5.8 ± 0.6	2.0 ± 0.2	0.6 ± 0.07
NGC 3628	2.1 ± 0.4	4.8 ± 0.5	54.8 ± 5.6	50.6 ± 5.1	52.0 ± 5.2	67.8 ± 6.8	29.1 ± 2.9	10.8 ± 1.1	3.1 ± 0.32
NGC 3627	...	8.6 ± 0.9	66.3 ± 6.7	15.2 ± 1.5	22.8 ± 2.3	19.0 ± 1.9	7.0 ± 0.7	2.5 ± 0.3	0.8 ± 0.08
IRAS 18293–3413	3.1 ± 0.3	4.0 ± 0.4	35.7 ± 3.6	42.8 ± 4.3	55.1 ± 5.5	42.6 ± 4.3	15.0 ± 1.5	5.6 ± 0.6	1.5 ± 0.16
NGC 7469	4.6 ± 0.5	6.0 ± 0.6	27.3 ± 2.8	28.9 ± 3.1	32.9 ± 3.7	23.3 ± 2.8	8.2 ± 1.0	2.9 ± 0.4	0.7 ± 0.10
IRAS 17578–0400	0.7 ± 0.1	1.1 ± 0.2	27.7 ± 3.0	31.4 ± 3.3	34.5 ± 3.7	23.3 ± 2.6	8.5 ± 1.0	3.0 ± 0.4	0.8 ± 0.10
IC 1623	2.7 ± 0.3	3.6 ± 0.4	22.9 ± 2.4	24.6 ± 2.5	27.6 ± 2.8	20.3 ± 2.4	7.3 ± 0.7	2.7 ± 0.3	0.7 ± 0.08
Arp 220	5.3 ± 0.5	8.0 ± 0.8	104.1 ± 10.5	132.8 ± 13.4	...	83.3 ± 8.4	30.6 ± 3.1	10.7 ± 1.1	3.7 ± 0.39
IRAS 19254–7245	1.1 ± 0.1	1.4 ± 0.2	5.2 ± 0.6	5.5 ± 0.6	5.8 ± 0.6	4.1 ± 0.4	1.5 ± 0.2	0.5 ± 0.1	0.1 ± 0.02

Note. The flux densities of the MIPS, PACS, and SPIRE maps are extracted at the same positions as the APEX pointings. We first convolve their native angular resolutions to the same beam size as our APEX observations and scale the map units to janskys per beam by a factor of $\pi/4\,ln\,2 \times (\mathrm{HPBW_{beam}/pixelsize})^2$. The IRAS data are taken from Sanders et al. (2003) as flux densities of the entire galaxies.

Table 4
Derived Molecular Properties and Fitting Results

Source Name	$L'_{\rm HCN\,2-1}$ (10^7 K km s^{-1} pc^2)	$L'_{\rm HCO^+\,2-1}$ (10^7 K km s^{-1} pc^2)	$L_{\rm IR}$ ($10^9\,L_\odot$)	$T_{\rm c}$ (K)	β_c	$T_{\rm w}$ (K)	$M_{\rm dense}^{\rm HCN}$ ($10^8\,M_\odot$)	$M_{\rm dense}^{\rm HCO^+}$ ($10^8\,M_\odot$)	SFR$_{\rm IR}$ ($M_\odot$ yr^{-1})
(1)	(2)	(3)	(4)	(5)	(6)	(7)	(8)	(9)	(10)
NGC 4945	1.7 ± 0.4	1.6 ± 0.4	19.0 ± 0.8	23 ± 1	2.4 ± 0.2	49 ± 2	1.8 ± 0.4	1.8 ± 0.4	3.5 ± 0.4
NGC 1068	3.2 ± 1.6	2.4 ± 1.2	42.3 ± 3.1	28 ± 1	2.1 ± 0.1	74 ± 10	3.4 ± 1.8	2.5 ± 1.3	7.3 ± 1.1
NGC 7552	1.8 ± 0.5	2.4 ± 0.7	40.0 ± 2.3	23 ± 2	2.5 ± 0.2	62 ± 2	1.9 ± 0.6	2.7 ± 0.7	7.9 ± 1.2
NGC 4418	4.0 ± 1.3	2.8 ± 1.0	55.2 ± 2.7	30 ± 4	1.8 ± 0.2	62 ± 2	4.3 ± 1.3	3.1 ± 1.0	9.6 ± 1.4
NGC 1365	3.8 ± 1.9	2.8 ± 1.5	69.7 ± 3.3	22 ± 1	2.3 ± 0.2	58 ± 2	4.2 ± 2.1	3.0 ± 1.6	12.2 ± 1.7
NGC 3256	10.4 ± 4.6	19.0 ± 8.1	351 ± 18	25 ± 2	2.4 ± 0.2	62 ± 3	11.2 ± 5.1	20.6 ± 8.8	53.3 ± 8.1
NGC 1808	1.1 ± 0.6	1.1 ± 0.6	20.7 ± 0.8	23 ± 2	2.5 ± 0.2	61 ± 2	1.2 ± 0.6	1.2 ± 0.6	3.5 ± 0.5
IRAS 13120–5453	97 ± 36	87 ± 35	1517 ± 79	25 ± 2	2.4 ± 0.2	54 ± 2	106 ± 39	94 ± 37	243.5 ± 36.7
IRAS 13242–5713	10.3 ± 3.4	19.5 ± 5.3	258 ± 14	24 ± 2	2.4 ± 0.2	55 ± 2	11.2 ± 3.7	21.2 ± 5.7	41.4 ± 6.2
Mrk 331	10.7 ± 4.6	<11.1	125.0 ± 6.5	23 ± 2	2.5 ± 0.2	59 ± 2	11.6 ± 4.9	<11.9	21.3 ± 3.1
NGC 6240	80 ± 30	107 ± 36	586 ± 35	25 ± 2	2.3 ± 0.2	60 ± 2	87 ± 32	117 ± 39	95 ± 15
NGC 3628	0.6 ± 0.2	0.8 ± 0.2	11.7 ± 0.5	17 ± 1	2.8 ± 0.2	51 ± 1	0.6 ± 0.3	0.9 ± 0.3	2.2 ± 0.3
NGC 3627	0.7 ± 0.3	<0.8	2.7 ± 0.1	23 ± 1	2.4 ± 0.1	57 ± 3	0.7 ± 0.3	<0.9	0.7 ± 0.1
IRAS 18293–3413	25 ± 10	42 ± 13	521 ± 25	23 ± 2	2.4 ± 0.2	58 ± 2	26.7 ± 11.3	46 ± 15	83 ± 12
NGC 7469	<22.4	17.8 ± 6.3	250 ± 16	23 ± 2	2.4 ± 0.2	63 ± 3	<24.3	19.3 ± 6.9	41.8 ± 6.4
IRAS 17578–0400	<17.4	<14.9	205 ± 10	23 ± 2	2.4 ± 0.2	48 ± 1	<18.8	<16.1	32.8 ± 4.8
IC 1623	<26.0	25 ± 10	350 ± 19	23 ± 2	2.4 ± 0.2	60 ± 2	<28.2	27.0 ± 11.3	59.1 ± 8.9
Arp 220	138 ± 36	70 ± 19	1650 ± 65	31 ± 3	1.7 ± 0.1	56 ± 4	151 ± 39	76 ± 21	258 ± 39
IRAS 19254–7245	58.9 ± 6.3	37.5 ± 4.3	1153 ± 97	22 ± 2	2.6 ± 0.2	64 ± 2	64 ± 15	40.7 ± 9.9	171 ± 27

Note. Column 1: galaxy name. Column 2: HCN $J = 2 \rightarrow 1$ line luminosity. Column 3: HCO$^+$ $J = 2 \rightarrow 1$ line luminosity. Column 4: total IR luminosity. Column 5: cold component dust temperature. Column 6: cold component dust emissivity index. Column 7: warm component dust temperature. Column 8: dense gas mass derived from HCN $J = 2 \rightarrow 1$. Column 9: dense gas mass derived from HCO$^+$ $J = 2 \rightarrow 1$. Column 10: SFR derived from IR luminosity.

estimation of the dense gas mass relies on both brightness temperature and density, where we adopt $T_{\rm b} \sim 35$ K and $\langle n({\rm H_2})\rangle = 3 \times 10^4$ cm^{-3} for the typical conditions of Galactic virialized cloud cores (Radford et al. 1991). There are few HCN $J = 2 \rightarrow 1$ and HCO$^+$ $J = 2 \rightarrow 1$ observations in the literature (e.g., Immer et al. 2016). Therefore, we can derive an average HCN $J = 2 \rightarrow 1$/HCN $J = 1 \rightarrow 0$ $T_{\rm b}$ from HCN $J = 3 \rightarrow 2$/HCN $J = 1 \rightarrow 0$ ratios with RADEX by assuming the above physical conditions. We adopt the average HCN $J = 3 \rightarrow 2$/HCN $J = 1 \rightarrow 0$ $T_{\rm b}$ ratio of $\sim 0.26 \pm 0.10$ found in Galactic dense cores (Wu et al. 2010), and the derived HCN $J = 2 \rightarrow 1$/HCN $J = 1 \rightarrow 0$ $T_{\rm b}$ ratio is ~ 0.67, which is further adopted to convert from luminosity to the dense gas mass. We derive the dense gas mass traced by HCO$^+$ with the same method by assuming that the two lines have similar excitations. The derived dense gas mass ranges from 4×10^7 to $10^{10}\,M_\odot$.

Following Tan et al. (2018), we adopt the SFR conversion calibrated by Kennicutt (1998a) and Murphy et al. (2011):

$$\left(\frac{\rm SFR}{M_\odot\,{\rm yr}^{-1}}\right) = 1.50 \times 10^{-10}\left(\frac{L_{\rm IR}}{L_\odot}\right). \quad (8)$$

The SFR is calculated based on the Kroupa (2001) initial mass function (IMF). The derived gas mass and SFR are shown in Table 4.

4. Results

4.1. Spectra

We present APEX spectra of HCN $J = 2 \rightarrow 1$ and HCO$^+$ $J = 2 \rightarrow 1$ in Figure 1. In total, we detect 14 HCN $J = 2 \rightarrow 1$ and 14 HCO$^+$ $J = 2 \rightarrow 1$ lines with their velocity-integrated line intensities, $I > 3\sigma$. Twelve galaxies have detections of both HCN $J = 2 \rightarrow 1$ and HCO$^+$ $J = 2 \rightarrow 1$. Object IRAS 17578–0400 was not detected in either of the two lines, and NGC 7469 and IC 1623 were not detected only in HCN $J = 2 \rightarrow 1$, possibly because of their large distances. On the other hand, HCO$^+$ $J = 2 \rightarrow 1$ is only marginally detected on $\sim 3\sigma$ levels in these two galaxies. Objects Mrk 331 and NGC 3627 have nondetections of HCO$^+$ $J = 2 \rightarrow 1$. The velocity-integrated fluxes of all galaxies are shown in Table 2. We show 3σ upper limits for those nondetected lines.

4.2. Correlation between Luminosities of Dense Gas Tracers and IR Emission

In Figure 2, we present the $L_{\rm IR} - L'_{\rm dense}$ correlation using HCN $J = 2 \rightarrow 1$ and HCO$^+$ $J = 2 \rightarrow 1$ line luminosities, which trace the total dense gas mass. We fit linear regressions with the methods of orthogonal least squares (OLS) and MCMC to avoid possible bias from the fitting algorithm. The OLS was fitted with an IDL Astrolibrary SIXLIN, which adopts orthogonal distances from data points to the fit line. The code first assumes a linear slope to compute orthogonal distance and then performs linear regression steps to compare with previous slopes until it reaches a steady state. We perform the MCMC method using the Python package EMCEE. We first employ 64 walkers, and each of them samples 5000 steps. This will ensure that most sampling is convergent. Then we burn them in and perform another 10,000 steps for each walker. This will offer a final sampling number of 640,000 for statistics. We adopt the range encompassing 68% of the data about the median of the posterior probability density distribution to represent approximate upper and lower 1σ limits for Gaussian-like distributions. These fitted results from the two methods are shown in Figure 2, without significant differences between each other. The slope obtained from OLS fitting is within the 1σ range of that from the Bayesian fitting.

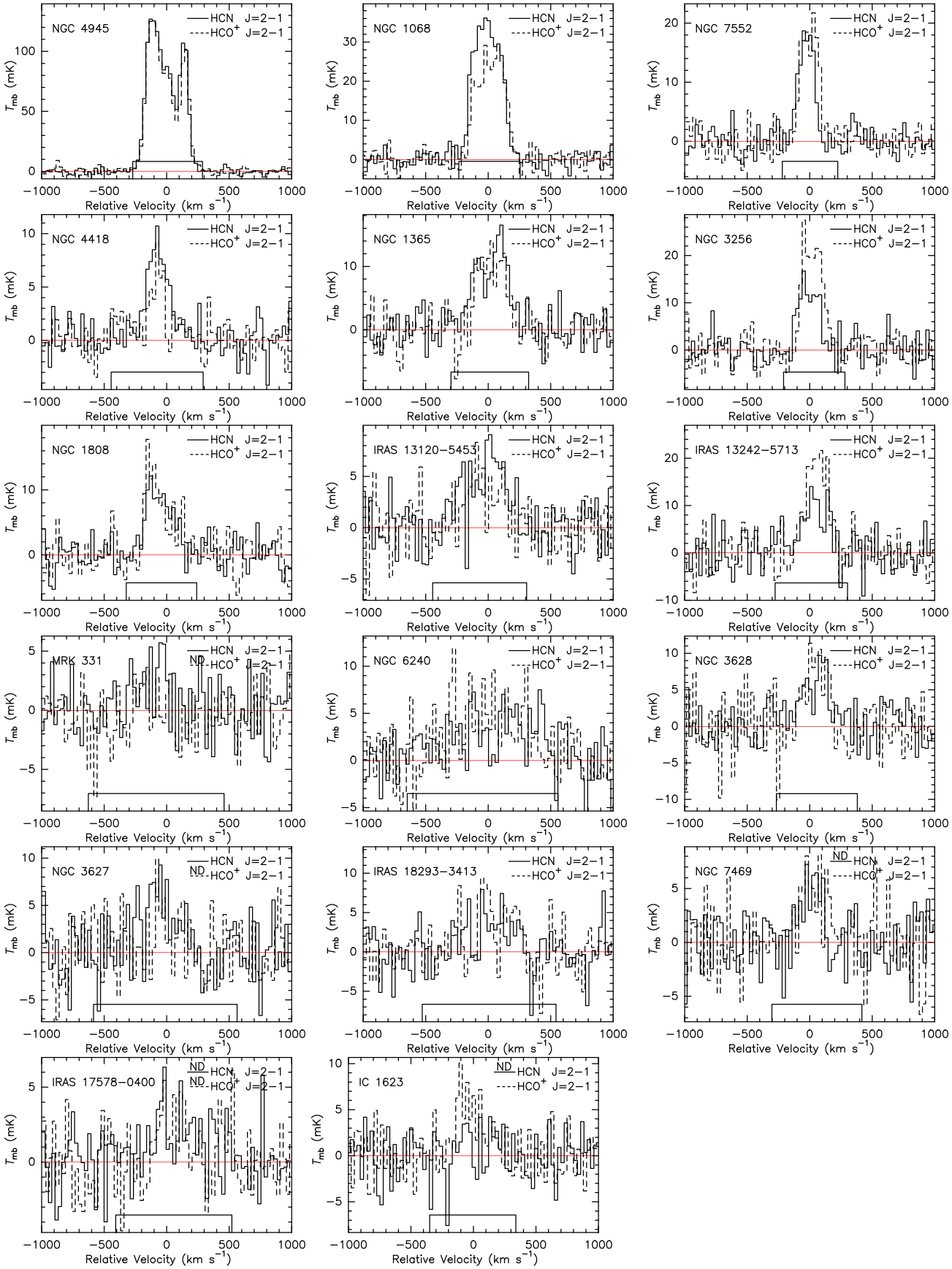

Figure 1. The HCN $J = 2 \rightarrow 1$ and HCO^+ $J = 2 \rightarrow 1$ spectra of 17 galaxies observed with the APEX 12 m telescope. Solid and dashed lines show the line profiles of HCN $J = 2 \rightarrow 1$ and HCO^+ $J = 2 \rightarrow 1$, respectively. We detect both lines in 12 galaxies. Five sources only have one detected line with a velocity-integrated line intensity $>3\sigma$. The nondetections are tagged as "ND" above the line labels.

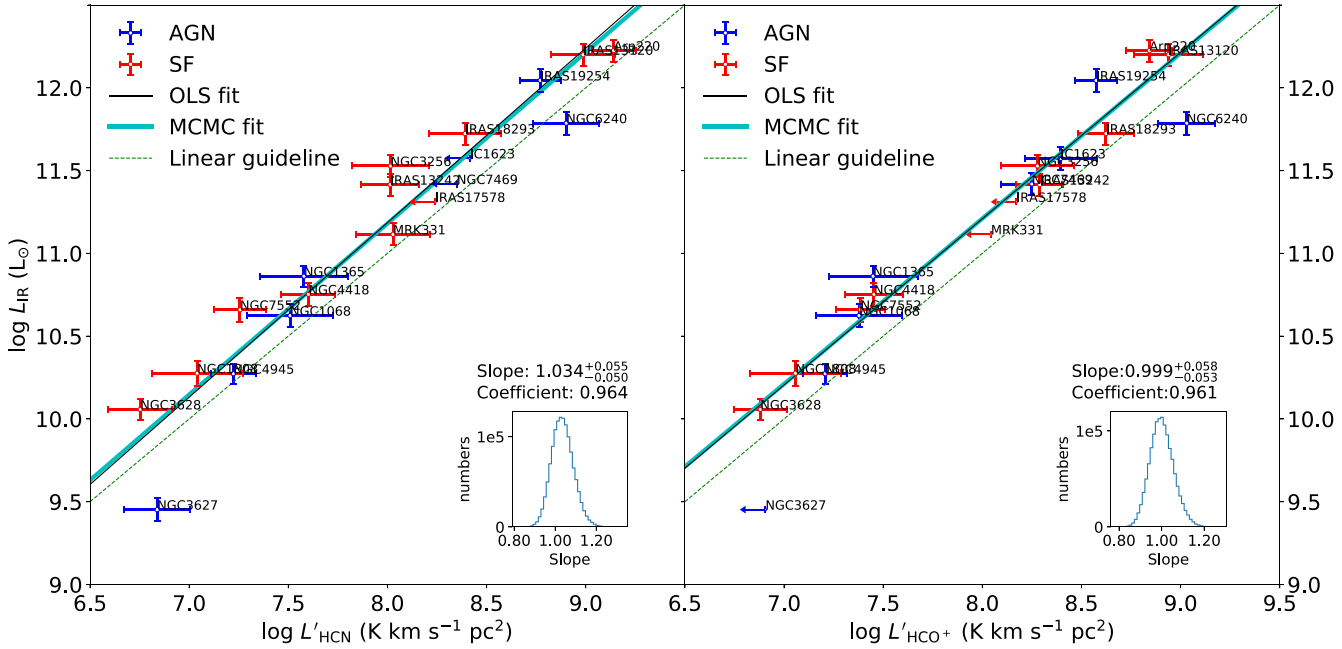

Figure 2. Left: correlation between $L'_{\rm HCN\,J=2\rightarrow1}$ and $L_{\rm IR}$. Right: correlation between $L'_{\rm HCO^+\,J=2\rightarrow1}$ and $L_{\rm IR}$. The AGN- and SF-dominated galaxies are shown in blue and red points, respectively. The fitting results of OLS and MCMC are shown in black and cyan lines, respectively. The green dashed line shows a linear relation for reference. The insets present the probability density distributions of the slope sampling.

We find linear correlations between $L_{\rm IR}$ and $L'_{\rm HCNJ=2\rightarrow1}$ and $L'_{\rm HCO^+J=2\rightarrow1}$. The Pearson correlation efficiencies, which quantify linear correlations, are 0.96 and 0.97 with p-values of 1.7×10^{-9} and 2.0×10^{-10}, respectively. The Spearman correlation efficiencies, which quantify monotone correlations, are 0.98 and 0.96 with p-values of 1.0×10^{-10} and 4.8×10^{-9}, respectively. The AGN- and SF-dominated galaxies are shown in blue and red points, respectively. The MCMC fitting results are listed as follows:

$$\log L_{\rm IR} = 1.034^{+0.055}_{-0.051}\log L'_{\rm HCN\,2-1} + 2.91^{+0.4}_{-0.4}, \quad (9)$$

$$\log L_{\rm IR} = 1.000^{+0.058}_{-0.054}\log L'_{\rm HCO^+\,2-1} + 3.21^{+0.43}_{-0.47}, \quad (10)$$

where the upper and lower errors are from the probability density distributions of the parameters. Nondetections are not included during fitting. We find no definite difference between AGN- and SF-dominated galaxies, which essentially follow the same trend of $L_{\rm IR}$ and $L'_{\rm dense}$.

4.3. Correlations of Luminosity Surface Densities

Here we derive luminosity surface densities by adopting the area measured from the 1.4 GHz radio continuum images, which can eliminate the degeneracy introduced by the distance in the luminosity correlations. The 1.4 GHz radio emission, which is contributed both by the synchrotron emission from supernova remnants and by the free–free emission from H II regions, originates from the same star-forming regions as the IR emission (Bell 2003). There exist rich archival radio data at high angular resolutions that would help determine the 1.4 GHz continuum sizes (see details in Section 2.4).

The correlations between the surface densities of the IR luminosity ($\Sigma_{L_{\rm IR}}$) and dense gas tracer line luminosity ($\Sigma_{L'_{\rm dense}}$) are shown in Figure 3. The MCMC fitting results are as follows:

$$\log\Sigma_{L_{\rm IR}} = 0.987^{+0.032}_{-0.030}\log\Sigma_{L'_{\rm HCN\,2-1}} + 3.21^{+0.09}_{-0.09}, \quad (11)$$

$$\log\Sigma_{L_{\rm IR}} = 1.017^{+0.035}_{-0.034}\log\Sigma_{L'_{\rm HCO^+\,2-1}} + 3.17^{+0.09}_{-0.10}, \quad (12)$$

where $\Sigma_L = L/(2\pi r_{\rm RC}^2)$ is the luminosity surface density. The fitted slope indices of HCN $J=2\rightarrow1$ and HCO$^+$ $J=2\rightarrow1$ are 0.99 and 1.02, respectively. Both the OLS and MCMC methods give identical fitting results. The Pearson correlation efficiencies are 0.99 and 0.99 with p-values of 2.7×10^{-12} and 1.8×10^{-13} for HCN $J=2\rightarrow1$ and HCO$^+$ $J=2\rightarrow1$, respectively. The Spearman correlation efficiencies of these two lines are 0.99 and 0.98 with p-values of 8.1×10^{-13} and 1.0×10^{-10}, respectively. Both correlation coefficients are higher than those obtained from the luminosity relations, showing much tighter correlations in the surface density relations.

Scatters in the surface density correlations are 0.150 and 0.113 dex for HCN and HCO$^+$ $J=2\rightarrow1$, respectively. These values are very close to the scatters in the luminosity correlations (0.147 and 0.113 dex). This is likely because the surface density correlations have larger dynamic ranges, and both types of correlations share the same physical origin.

4.4. SF Efficiency of Dense Molecular Gas

Using HCN and HCO$^+$ $J=4\rightarrow3$ transitions in nearby star-forming galaxies, Tan et al. (2018) found that $L_{\rm IR}/L'_{\rm dense}$, which is a proxy of dense gas SF efficiency (SFE), increases with $L_{\rm IR}$ within individual galaxies but not for galaxy-integrated ratios. Furthermore, there seems to also be a correlation between $L_{\rm IR}/L'_{\rm dense}$ and the PACS 70/100 μm ratio (as a proxy of warm dust temperature).

To further verify these trends, we plot SFE (derived from $L_{\rm IR}/L'_{\rm HCN}$ and $L_{\rm IR}/L'_{\rm HCO^+}$) as a function of IR luminosity in Figure 4. Our data do not show any statistical correlation in the SFE–$L_{\rm IR}$ diagram with Spearman correlation p-values of 0.99 and 0.85 for HCN $J=2\rightarrow1$ and HCO$^+$ $J=2\rightarrow1$, respectively (see Table 4), meaning that the data have a high chance

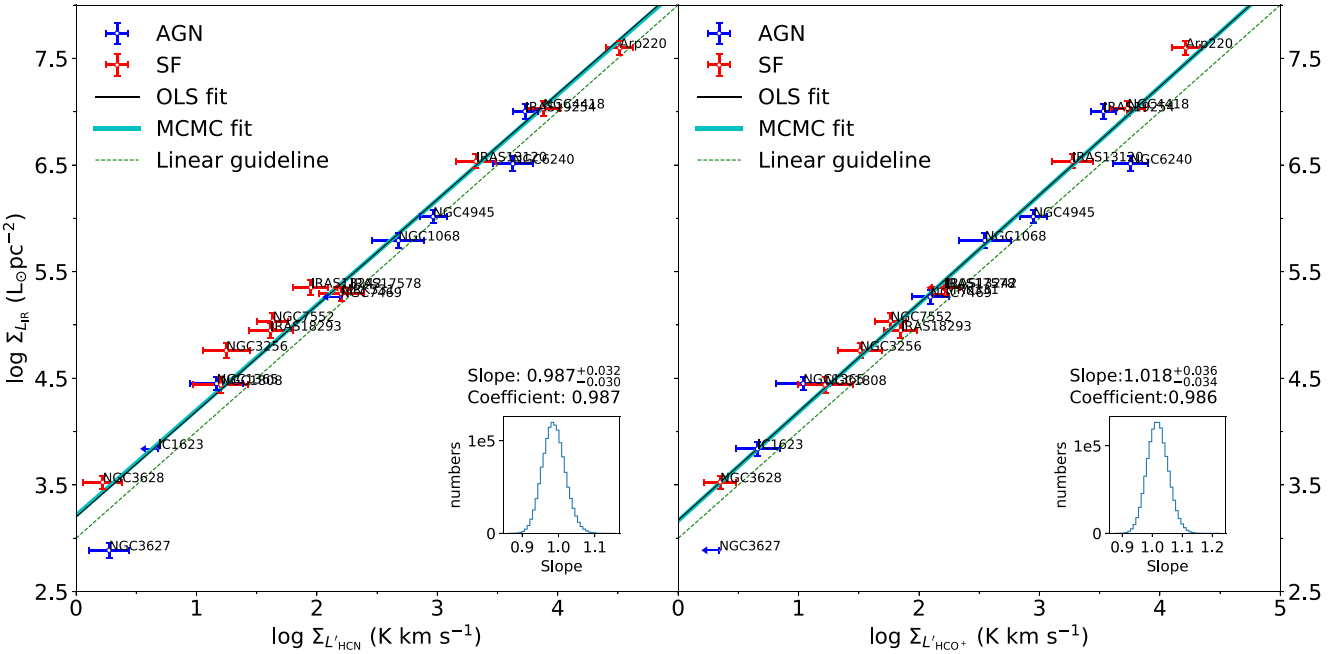

Figure 3. Left: correlation between $\Sigma_{L'_{\rm HCN\ J=2\rightarrow1}}$ and $\Sigma_{L_{\rm IR}}$. Right: correlation between $\Sigma_{L'_{\rm HCO^+\ J=2\rightarrow1}}$ and $\Sigma_{L_{\rm IR}}$. The AGN- and SF-dominated galaxies are shown in blue and red points, respectively. The fitting results of OLS and MCMC are shown in black and cyan lines, respectively. The green dashed line shows a linear relation for reference. The insets present the probability density distributions of the fitted slopes.

to distribute randomly. These are consistent with the integrated results of Tan et al. (2018).

In general, SFE obtained from HCN and HCO^+ seems to be confined within a small range, with scatters of only 0.19 and 0.16. These small scatters are even less than that of HCN $J=1\rightarrow0$ ($\sim$0.25 found in $L_{\rm IR}/L_{\rm HCN\ 1-0}$; Gao & Solomon 2004a). This indicates that the $J=2\rightarrow1$ transitions of HCN and HCO^+ are more robust in tracing the dense gas mass in galaxies. However, the $L_{\rm IR}/L_{\rm HCN\ 4-3}$ ratios have a much more divergent range of almost 2 orders of magnitude (Tan et al. 2018).

Unlike Tan et al. (2018), on the other hand, the SFE–$T_{\rm c}$ diagram also does not show any correlations, with Spearman correlation p-values of 0.46 and 0.91 for HCN $J=2\rightarrow1$ and HCO^+ $J=2\rightarrow1$, respectively. The $J=4\rightarrow3$ transitions are more sensitive to the dust temperature because they need a very high density and relatively high temperature to be excited. These make them trace the dense gas close to young massive stars, instead of the global properties cold dense cores traced by the $J=2\rightarrow1$ and $J=1\rightarrow0$ transitions.

4.5. Ratios of $L'_{\rm HCN\ J=2\rightarrow1}/L'_{\rm HCO^+\ J=2\rightarrow1}$

Figure 5 presents the line ratio of $L'_{\rm HCN}/L'_{\rm HCO^+}$ as a function of IR luminosity surface density and cold dust temperature. We also overlay the HCN and HCO^+ $J=1\rightarrow0$ ratios collected from the literature (Nguyen et al. 1992; Solomon et al. 1992; Gao & Solomon 2004b; Wang et al. 2004; García-Burillo et al. 2006; Baan et al. 2008; Krips et al. 2008). There seems to be no systematic difference between the ratios of both HCN/HCO^+ $J=1\rightarrow0$ and HCN/HCO^+ $J=2\rightarrow1$. The average $J=1\rightarrow0$ ratio is 1.25 ± 0.42, and the $J=2\rightarrow1$ ratio is 1.05 ± 0.42. The $J=1\rightarrow0$ ratio is higher, and the difference is smaller than the scatter.

The ratio of $L'_{\rm HCN}/L'_{\rm HCO^+}$ may be changed by variation from astrochemistry (Lintott & Viti 2006; Imanishi et al. 2007), molecular excitation (García-Burillo et al. 2006), radiative transfer (Knudsen et al. 2007), metallicities (Liang et al. 2006), and many other processes. The temperature and IR luminosity of dust grains would reflect the energy from young stars and their surrounding dense gas. Therefore, here we try to find a possible dependence of this ratio on SF intensity (traced by the IR luminosity surface density) and cold dust temperature. We choose the temperature of the cold dust component because (1) it comes from the bulk of the galactic dust composition, taking the majority of the dust mass (>95%; e.g., Appendix B); (2) it is well sampled in our SED fitting (e.g., Figure 10); and (3) it contributes the majority of the far-IR luminosity, which has an excellent correlation with the total IR luminosity (e.g., Zhu et al. 2008).

The average ratios of HCN/HCO^+ $J=2\rightarrow1$ are 1.15 ± 0.26 and 0.98 ± 0.42 for AGN- and SF-dominated galaxies, respectively. Though it seems that AGN-dominated galaxies may systematically have higher HCN/HCO^+ line ratios, the difference is still within 1σ. There seems to also exist a weak trend between line ratio and dust temperature. But if we remove the data points of NGC 3628 and Arp 220, this trend disappears.

4.6. Dense Gas Fraction in Galaxies

The ratios of $L'_{\rm HCN}/L'_{\rm CO}$ and $L'_{\rm HCO^+}/L'_{\rm CO}$ would roughly trace the dense gas fraction in galaxies, albeit the large uncertainties of the conversion factors in both CO and dense gas tracers. Similar to what was found in the $J=1\rightarrow0$ transition of HCN in Gao & Solomon (2004a), the ratios of $L'_{\rm HCN}/L'_{\rm CO}$ and $L'_{\rm HCO^+}/L'_{\rm CO}$ both show increasing trends as a function of $L_{\rm IR}$ and $\Sigma_{L_{\rm IR}}$ (Figure 6). The Pearson correlation coefficient between the $L'_{\rm HCN\ J=2\rightarrow1}/L'_{\rm CO\ J=1\rightarrow0}$ ratio and IR surface density is 0.81 (p-value $=2.4\times10^{-4}$), which is higher than that of the $L'_{\rm HCO^+\ J=2\rightarrow1}/L'_{\rm CO\ J=1\rightarrow0}$ ratio (0.49,

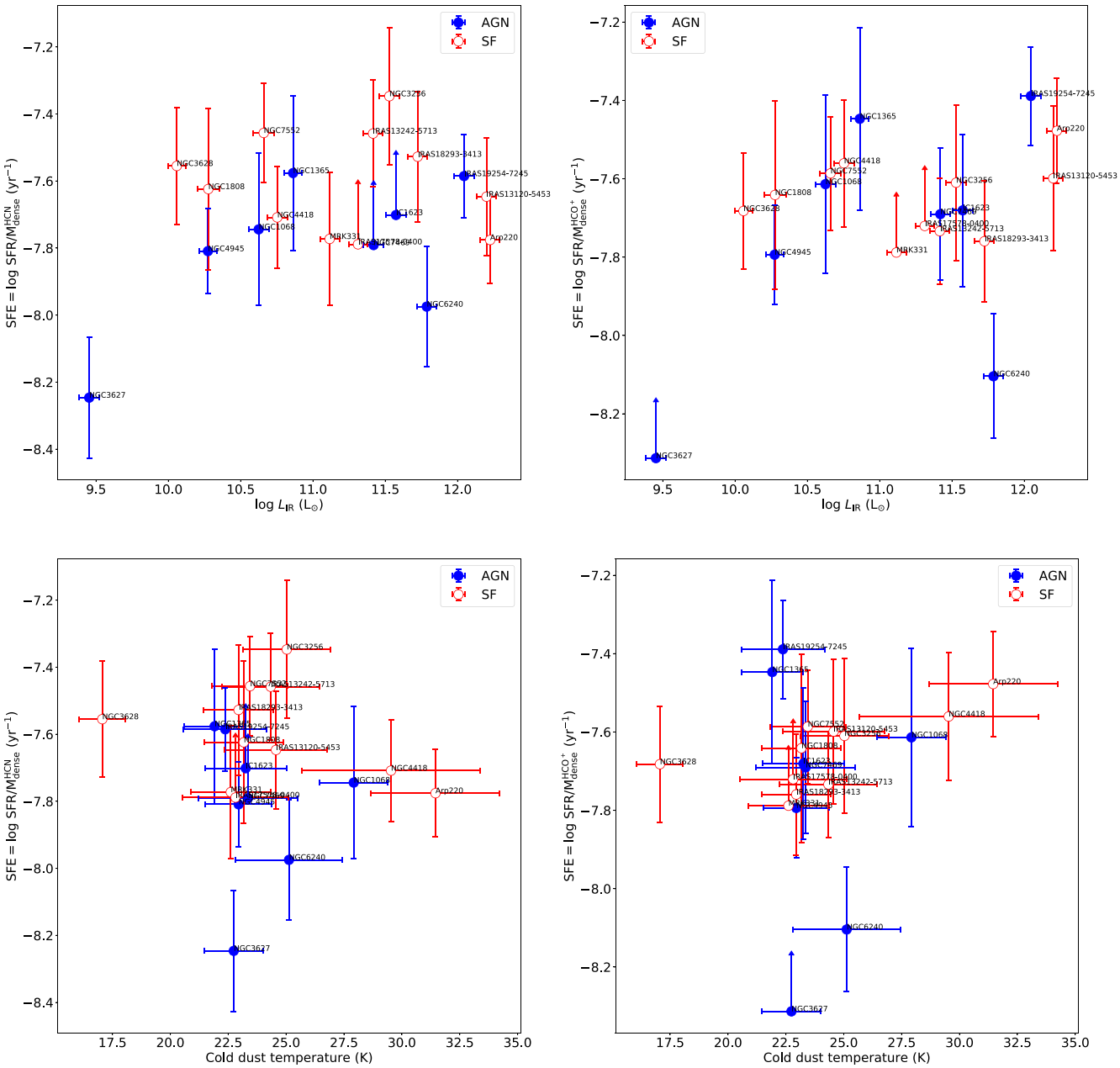

Figure 4. Top left: SFR/$M_{\rm dense}$ traced by HCN $J = 2 \rightarrow 1$ as a function of IR luminosity. Top right: SFR/$M_{\rm dense}$ traced by HCO^+ $J = 2 \rightarrow 1$ as a function of IR luminosity. Bottom left: SFR/$M_{\rm dense}$ traced by HCN $J = 2 \rightarrow 1$ as a function of cold dust temperature. Bottom right: SFR/$M_{\rm dense}$ traced by HCN $J = 2 \rightarrow 1$ as a function of cold dust temperature. The AGN- and SF-dominated galaxies are shown in blue and red points, respectively.

p-value $= 0.064$), indicating that HCN/CO ratios might be more robust in tracing dense gas fractions.

These are also consistent with the positive correlations between the $L'_{\rm HCN\,1-0,3-2}/L'_{\rm CO\,1-0}$ ratio and $L_{\rm IR}$ (e.g., Juneau et al. 2009, who found a better correlation for the $J = 3 \rightarrow 2$ transition than that of $J = 1 \rightarrow 0$, indicating an increased molecular gas density in more IR-bright galaxies).

We summarize the statistics parameters of the correlations and list all of them in Table 5, including the MCMC fitting results, OLS fitting results, Pearson (linear relation) ordered correlation coefficient and p-value, Spearman (monotonic relation) ordered correlation coefficient and p-value, and scatter of diversions from the OLS fitting.

The correlations of luminosities ($L'_{\rm dense} - L_{\rm IR}$) and luminosity surface densities ($\Sigma_{L'_{\rm dense}} - \Sigma_{L_{\rm IR}}$) all show significant correlation (Spearman p-value $< 10^{-8}$). The correlations of $L'_{\rm HCN}/L'_{\rm CO} - \Sigma_{L_{\rm IR}}$, $L'_{\rm HCN}/L'_{\rm HCO^+} - \Sigma_{L_{\rm IR}}$, and $T_{\rm c} - \Sigma_{L_{\rm IR}}$ are also statistically valid with p-values < 0.05 for both Pearson and Spearman rank. Those noncorrelated relations show large error bars of linear fitting and large p-values (>0.05) and sometimes also large differences between the results from MCMC and OLS.

5. Discussion

We adopt the total IR luminosity (integrated from 3 to 1000 μm) as the SFR tracer of galaxies. The $L_{\rm IR}$ has been widely used as an SFR tracer, while it still has some limitations. The AGNs may contribute to mid-IR emission by their hot dusty tori (Padovani et al. 2017); thus, $L_{\rm IR}$ may overestimate SFR in strong AGN-dominated galaxies. On the other hand,

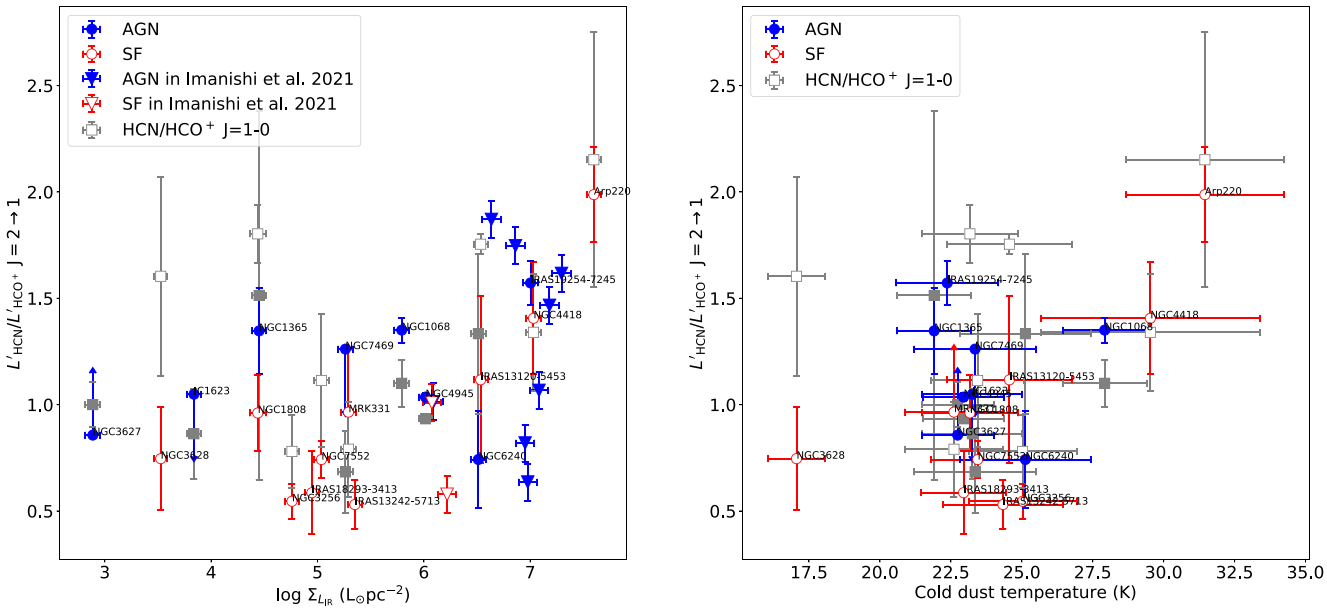

Figure 5. Left: ratio of $L'_{\rm HCN}/L'_{\rm HCO^+}$ $J=2\rightarrow1$ as a function of IR luminosity surface density. Right: ratio of $L'_{\rm HCN}/L'_{\rm HCO^+}$ $J=2\rightarrow1$ as a function of cold component dust temperature. The sample in this work is shown with circles, while the ALMA ULIRG sample from Imanishi et al. (2022) is shown with triangles. The AGN-dominated galaxies are shown with blue filled points, and SF-dominated galaxies are shown with red open points. The gray square points are HCN and HCO^+ $J=1\rightarrow0$ from the literature for comparison (Nguyen et al. 1992; Solomon et al. 1992; Gao & Solomon 2004b; Wang et al. 2004; García-Burillo et al. 2006; Baan et al. 2008; Krips et al. 2008).

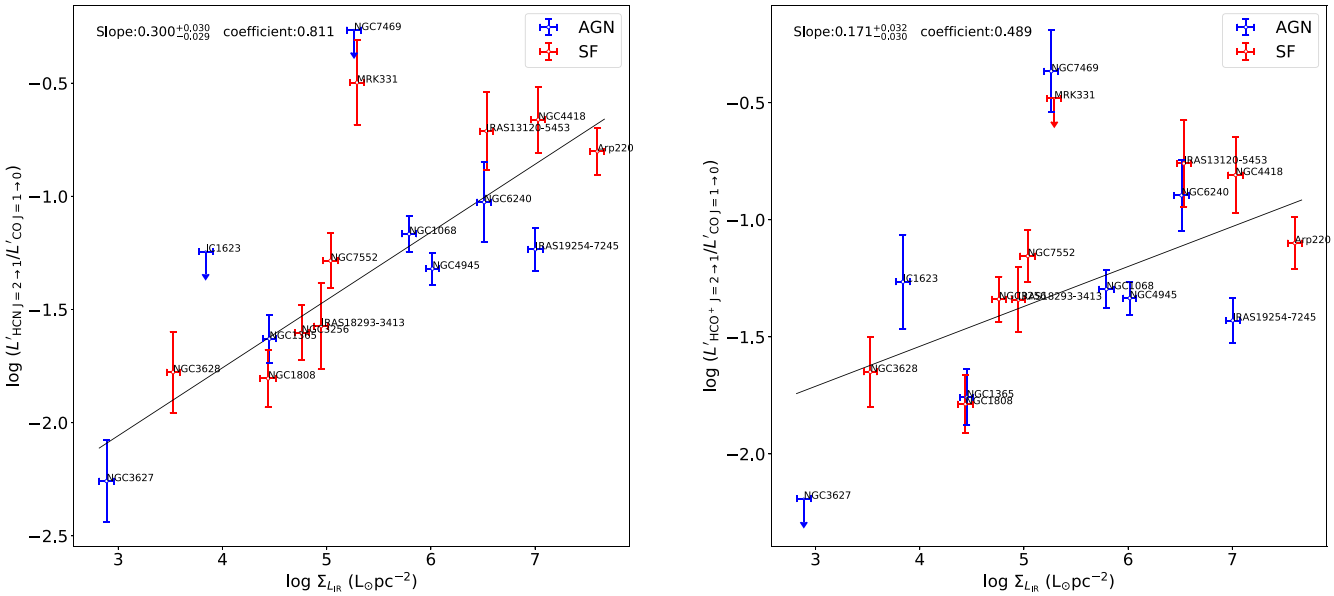

Figure 6. Left: $L'_{\rm HCN}/L'_{\rm CO}$ as a function of IR surface density. Right: $L'_{\rm HCO^+}/L'_{\rm CO}$ as a function of IR surface density. The AGN- and SF-dominated galaxies are shown with blue filled points and red open points, respectively. The best-fit results are shown with solid lines. Nondetections are not included in the fitting.

$L_{\rm IR}$ traces SFR on relatively long timescales up to 200 Myr (Kennicutt & Evans 2012), and it may significantly overestimate the instantaneous SFR of recent-quenched galaxies (Hayward et al. 2014). When converting from gas luminosity to dense gas mass, we assume that all molecular lines are collisionally excited. However, the IR-pumping mechanism may also contribute to the line excitation and could largely enhance HCN and HCO^+ emission. If the observed HCN and HCO^+ fluxes are dominated by IR pumping, the dense gas mass would be overestimated. Furthermore, variation in the stellar IMF between different galaxies would also bias the SFR calculation from $L_{\rm IR}$ (e.g., Jeřábková et al. 2017; Zhang et al. 2018).

The sizes of star-forming regions may be biased by the compact radio emission contributed by AGNs. Therefore, we collect VLBI high-resolution data from the literature (Cole et al. 1998; Roy et al. 1998; Smith et al. 1998; Lonsdale et al. 2003; Gallimore & Beswick 2004; Lenc & Tingay 2009; Deller & Middelberg 2014; Varenius et al. 2014) and determine if our measured sizes are severely biased by AGNs (see Table 1). For most galaxies, the central compact sources only contribute $\lesssim$10% of the total radio fluxes. Among all targets, NGC 7469

Table 5
Statistics Parameters of Different Fittings

	MCMC		OLS		Pearson		Spearman		
Fitting Name (1)	Slope (2)	Intercept (3)	Slope (4)	Intercept (5)	r_{xy} (6)	p-value (7)	r_{xy} (8)	p-value (9)	Scatter (10)
$L_{\rm IR} - L'_{\rm HCN}$	$1.03^{+0.05}_{-0.05}$	$2.9^{+0.4}_{-0.4}$	1.05 ± 0.04	2.8 ± 0.3	0.96	1.7×10^{-9}	0.98	1.0×10^{-10}	0.15
$L_{\rm IR} - L'_{\rm HCO^+}$	$1.00^{+0.06}_{-0.05}$	$3.2^{+0.4}_{-0.5}$	1.00 ± 0.03	3.2 ± 0.2	0.97	2.0×10^{-10}	0.96	4.8×10^{-9}	0.11
$\Sigma_{L_{\rm IR}} - \Sigma_{L'_{\rm HCN}}$	$0.99^{+0.03}_{-0.03}$	$3.21^{+0.09}_{-0.09}$	0.99 ± 0.02	3.20 ± 0.07	0.99	2.7×10^{-12}	0.99	8.1×10^{-13}	0.15
$\Sigma_{L_{\rm IR}} - \Sigma_{L'_{\rm HCO^+}}$	$1.02^{+0.04}_{-0.03}$	$3.17^{+0.09}_{-0.10}$	1.02 ± 0.01	3.17 ± 0.03	0.99	1.8×10^{-13}	0.98	1.0×10^{-10}	0.11
$L'_{\rm HCN}/L'_{\rm HCO^+} - \Sigma_{L_{\rm IR}}$	$0.33^{+0.04}_{-0.04}$	$-0.9^{+0.2}_{-0.2}$	0.30 ± 0.03	-0.7 ± 0.2	0.65	0.013	0.59	0.027	0.32
$L'_{\rm HCN}/L'_{\rm HCO^+} - T_{\rm c}$	$0.11^{+0.03}_{-0.26}$	$-1.6^{+6.1}_{-0.7}$	0.06 ± 0.01	-0.4 ± 0.3	0.53	0.053	0.21	0.47	0.36
$\rm SFR/M^{HCN}_{dense} - L_{IR}$	$0.02^{+0.05}_{-0.05}$	$-7.7^{+0.6}_{-0.5}$	0.03 ± 0.03	-7.8 ± 0.3	0.14	0.62	−0.003	0.99	0.19
$\rm SFR/M^{HCO^+}_{dense} - L_{IR}$	$0.01^{+0.05}_{-0.05}$	$-7.5^{+0.6}_{-0.6}$	-0.01 ± 0.02	-7.3 ± 0.3	−0.13	0.62	−0.053	0.85	0.16
$\rm SFR/M^{HCN}_{dense)} - T_c$	$-0.02^{+0.01}_{-0.01}$	$-7.1^{+0.3}_{-0.3}$	-0.016 ± 0.002	-7.07 ± 0.06	−0.26	0.33	−0.20	0.46	0.18
$\rm SFR/M^{HCO^+}_{dense} - T_c$	$0.00^{+0.01}_{-0.01}$	$-7.5^{+0.3}_{-0.3}$	0.003 ± 0.003	-7.52 ± 0.08	0.052	0.85	−0.029	0.91	0.16
$\rm SFR/M^{HCN}_{dense} - T_w$	$-0.005^{+0.008}_{-0.08}$	$-7.8^{+0.5}_{-0.5}$	0.003 ± 0.002	-7.63 ± 0.14	0.050	0.85	0.091	0.74	0.19
$\rm SFR/M^{HCO^+}_{dense} - T_w$	$0.007^{+0.008}_{-0.007}$	$-7.9^{+0.4}_{-0.5}$	0.006 ± 0.002	-7.79 ± 0.08	0.17	0.53	0.35	0.18	0.16
$L'_{\rm HCN}/L'_{\rm CO} - \Sigma_{L_{\rm IR}}$	$0.27^{+0.03}_{-0.03}$	$-2.8^{+0.2}_{-0.2}$	0.29 ± 0.02	-2.89 ± 0.09	0.81	2.4×10^{-4}	0.84	8.0×10^{-5}	0.27
$L'_{\rm HCO^+}/L'_{\rm CO} - \Sigma_{L_{\rm IR}}$	$0.10^{+0.03}_{-0.03}$	$-1.8^{+0.2}_{-0.2}$	0.13 ± 0.02	-2.0 ± 0.1	0.49	0.064	0.58	0.023	0.33
[a]$L_{\rm IR} - L'_{\rm HCN}$	$1.01^{+0.01}_{-0.01}$	$3.08^{+0.06}_{-0.06}$	1.010 ± 0.006	3.11 ± 0.05	0.997	4.2×10^{-26}	0.97	2.3×10^{-14}	0.17
[a]$L_{\rm IR} - L'_{\rm HCO^+}$	$1.082^{+0.008}_{-0.008}$	$2.56^{+0.04}_{-0.04}$	1.081 ± 0.005	2.57 ± 0.04	0.997	1.2×10^{-38}	0.95	3.6×10^{-18}	0.20
[a]$\Sigma_{L_{\rm IR}} - \Sigma_{L'_{\rm HCN}}$	$1.00^{+0.02}_{-0.01}$	$3.18^{+0.04}_{-0.04}$	0.993 ± 0.008	3.19 ± 0.02	0.99	1.4×10^{-21}	0.99	7.1×10^{-18}	0.16
[a]$\Sigma_{L_{\rm IR}} - \Sigma_{L'_{\rm HCO^+}}$	$1.10^{+0.01}_{-0.01}$	$2.90^{+0.02}_{-0.02}$	1.101 ± 0.009	2.92 ± 0.02	0.99	1.0×10^{-29}	0.97	2.6×10^{-21}	0.20
$T_{\rm c} - \Sigma_{L_{\rm IR}}$	$1.4^{+0.3}_{-0.3}$	16^{+2}_{-2}	3.5 ± 0.6	6 ± 3	0.67	0.002	0.55	0.015	0.87
$T_{\rm w} - \Sigma_{L_{\rm IR}}$	$0.9^{+0.4}_{-0.4}$	52^{+2}_{-2}	25 ± 50	-75 ± 260	0.13	0.58	0.091	0.71	1.20

Note. Column 1: fitting name. Column 2: slope fitted with MCMC. Column 3: intercept fitted with MCMC. Column 4: slope fitted with OLS. Column 5: intercept fitted with OLS. Column 6: Pearson rank-order correlation coefficient. Column 7: Pearson rank-order p-value. Column 8: Spearman rank-order correlation coefficient. Column 9: Spearman rank-order p-value. Column 10: scatter of diversion from the fitting.
[a] The fitting includes molecular clouds in the LMC and SMC.

has the highest AGN contribution, which is ∼18%. For the rest of the sample, most of them are classified as SF-dominated galaxies, so AGNs could not contribute much radio emission. For IRAS 19254–7245 and NGC 6240, we adopt the ALMA 250 and 480 GHz continuum to estimate star-forming region sizes, respectively.

5.1. SF Relation for Dense Gas Tracers

Our results show that SFR follows tight linear correlations with dense gas mass traced by both HCN $J = 2 \rightarrow 1$ and HCO^+ $J = 2 \rightarrow 1$, with slopes of 1.03 ± 0.05 and 1.00 ± 0.06, Pearson coefficients of 0.96 and 0.97, and dispersions of 0.15 and 0.11 dex, respectively (see Figure 2). The SF efficiencies are roughly constant (Pearson coefficients: 0.14 and −0.13) against SFR, with scatters of 0.19 and 0.16 dex (see Figure 4) for HCN $J = 2 \rightarrow 1$ and HCO^+ $J = 2 \rightarrow 1$, respectively. These suggest that dense gas clouds are direct sources of SF, while HCN $J = 2 \rightarrow 1$ and HCO^+ $J = 2 \rightarrow 1$ can be good tracers of dense molecular gas. On the other hand, we find no systematic variation between the slopes derived from the $J = 2 \rightarrow 1$ (1.03 ± 0.05) and $J = 1 \rightarrow 0$ (1.00 ± 0.05) transitions.

Two outliers that have deviated from the relationship of IR and dense gas tracer luminosity are NGC 6240 and NGC 3627. This makes their dense gas SF efficiencies, which are traced by the IR–to–dense gas luminosity ratio, about three times lower than the average value of other galaxies. This may indicate that the SFE of this dense gas is suppressed, or the dense gas tracer emission is enhanced by the extra heating mechanisms for the same star-forming activity. Starburst galaxy NGC 6240 is in the final merger stage (Tacconi et al. 1999; Iono et al. 2007; Papadopoulos et al. 2014; Kollatschny et al. 2020). The enormous shock condition across NGC 6240, shown both in the enhanced high-J CO lines and in large-scale shocked gas distribution (Meijerink et al. 2013; Lu et al. 2015; Cicone et al. 2018), could contribute mechanical heating to the dense gas, along with cosmic-ray and far-ultraviolet radiation from photon-dominated regions (Papadopoulos et al. 2014). These extreme conditions in NGC 6240 may also enhance the HCN $J = 2 \rightarrow 1$ and HCO^+ $J = 2 \rightarrow 1$ emission. Our observation of NGC 3627 is consistent with that of Murphy et al. (2015), who found that SFE in the nuclear region of NGC 3627 is several times lower than that in off-nuclear star-forming regions. This could explain why NGC 3627 also shows offsets from both HCN and HCO^+ $J = 2 \rightarrow 1$ correlations.

5.2. Connecting to Star-forming Clouds on Small Scales

The correlations obtained on large scales may have contamination from non-star-forming activities such as shock-enhanced line emission, diffuse gas components, etc. Therefore, it is necessary to check if the correlations can be extended to parsec scales that only contain star-forming dense molecular cores. Unfortunately, it is difficult to find systematic observations of the $J = 2 \rightarrow 1$ transition toward our Milky Way, while such observations do exist toward the Magellanic Clouds. Therefore, we compare the galaxy survey with the Magellanic Clouds data from Galametz et al. (2020), who presented

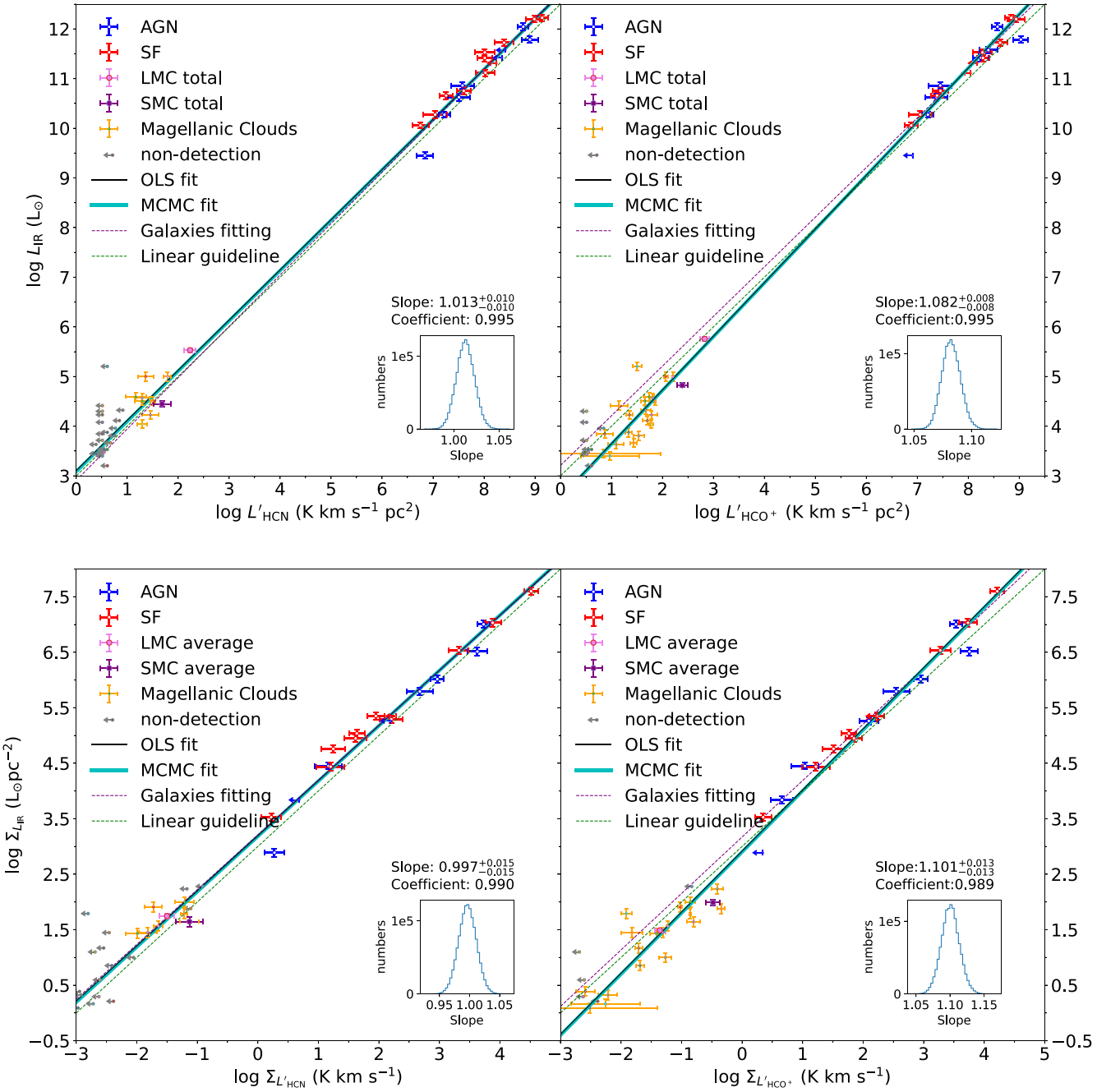

Figure 7. Top: correlations of $L'_{HCN} - L_{IR}$ (left) and $L'_{HCO^+} - L_{IR}$ (right). Bottom: correlations of $\Sigma_{L'_{HCN}} - \Sigma_{L_{IR}}$ (left) and $\Sigma_{L'_{HCO^+}} - \Sigma_{L_{IR}}$ (right). The correlations include dense molecular clouds from the Magellanic Clouds (Galametz et al. 2020), which are shown in orange circles. The total luminosity and averaged luminosity surface density of detected targets in the Magellanic Clouds are also shown for comparison. Luminosity upper limits of nondetection clouds are shown in gray arrows. The purple dashed lines are taken from Figures 2 and 3 and present the fitting results of galaxies.

HCN $J = 2 \rightarrow 1$ and HCO^+ $J = 2 \rightarrow 1$ observations toward ~30 LMC and SMC molecular clouds using APEX.

As shown in Figure 7, after including molecular clouds of the Magellanic Clouds in our galaxy sample, the correlations between $L'_{HCN\,J=2\rightarrow1}$–$L_{IR}$ and $L'_{HCO^+\,J=2\rightarrow1}$–$L_{IR}$ still hold with semilinear slopes of 1.021 and 1.088, respectively. The upper limits of nondetections seem off the correlation, possibly due to different detection criteria in Galametz et al. (2020), who considered a 3σ peak Gaussian fitting (instead of integrated flux) as the detection threshold. We also include data of the Magellanic Clouds in the correlations of surface densities by adopting the area from, e.g., Muller et al. (2010) and Wong et al. (2011). The obtained slopes are 1.00 and 1.10 for $\Sigma_{L'_{HCN}}$–$\Sigma_{L_{IR}}$ and $\Sigma_{L'_{HCO^+}}$–$\Sigma_{L_{IR}}$, respectively. Both HCN and HCO^+ data averaged (summed) across the Magellanic Clouds are shown in Figure 7 as individual data points, which seem to also follow the correlations of $\Sigma_{L'_{HCN}}$–$\Sigma_{L_{IR}}$ ($L'_{HCN\,J=2\rightarrow1}$–$L_{IR}$) and $\Sigma_{L'_{HCO^+}}$–$\Sigma_{L_{IR}}$ ($L'_{HCO^+\,J=2\rightarrow1}$–$L_{IR}$) found in galaxies.

On the other hand, we also simply overlay the Magellanic Clouds data with our fitted galaxy-only correlations. The HCN data from Magellanic Clouds well match with the correlation fitted in the galaxy-only sample, while the HCO^+ data from the Magellanic Clouds systematically lay below the fitted lines

Table 6
Line Fluxes from ALMA Observations

Source Name	Redshift	Distance (Mpc)	$S_{\mathrm{HCN}\,J=2\rightarrow1}$ (Jy km s^{-1})	$S_{\mathrm{HCO^+}\,J=2\rightarrow1}$ (Jy km s^{-1})	$\mathrm{HPBW_{dust}}$ (10^{-3} arcsec)	log L_{IR} ($L_\odot$)
(1)	(2)	(3)	(4)	(5)	(6)	(7)
NGC 1614	0.0160	68	11.56 ± 0.29	19.99 ± 0.31	1710×1630	11.7
IRAS 06035–7102	0.0795	356	3.77 ± 0.25	3.72 ± 0.29	705×613	12.2
IRAS 08572+3915	0.0580	256	1.44 ± 0.12	1.76 ± 0.13	318×287	12.1
IRAS 12112+0305	0.0730	326	8.63 ± 0.27	5.89 ± 0.28	283×186	12.3
IRAS 12127–1412	0.1332	620	0.79 ± 0.07	0.74 ± 0.08	151×96	12.2
IRAS 13509+0442	0.1364	636	1.25 ± 0.16	1.24 ± 0.19	481×367	12.3
IRAS 15250+3609	0.0552	243	4.31 ± 0.19	2.31 ± 0.19	445×375	12
Superantennae	0.0617	273	7.47 ± 0.54	4.27 ± 0.38	348×284	12.1
IRAS 20551–4250	0.0430	188	5.51 ± 0.03	8.67 ± 0.03	367×346	12
IRAS 22491–1808	0.0776	347	12.9 ± 0.36	8.00 ± 0.39	217×131	12.2

Note. Column 1: galaxy name. Column 2: redshifts from Imanishi et al. (2022). Column 3: luminosity distance from Imanishi et al. (2022). Column 4: HCN $J = 2 \rightarrow 1$ line flux we measured. Column 5: $\mathrm{HCO^+}$ $J = 2 \rightarrow 1$ line fluxed we measured. Column 6: galaxy sizes with HPBW of 178 GHz dust continuum from Imanishi et al. (2022). Column 7: logarithmic value of IR luminosity inferred from IRAS observation (Imanishi et al. 2022).

from galaxies, indicating a systematic $\mathrm{HCN/HCO^+}$ ratio variation possibly due to different metallicities.

5.3. $L'_{\mathrm{HCN}}/L'_{\mathrm{HCO^+}}J = 2 \rightarrow 1$ Ratio and Its Origins

The average of the HCN-to-$\mathrm{HCO^+}$ $J = 2 \rightarrow 1$ flux ratio of our sample is 1.15 ± 0.26 and 0.98 ± 0.42 for AGN-hosting and SF-dominated galaxies, respectively. Though it seems that the AGN-hosting galaxies may have relatively higher ratios than the SF-dominated galaxies, the difference is still within 1σ. So, we could not use this ratio to separate populations with AGNs. Our result of $J = 2 \rightarrow 1$ is consistent with that found in the $J = 1 \rightarrow 0$ lines (Privon et al. 2015; Li et al. 2020a).

Kohno et al. (2001) suggested that enhanced HCN emission originated from X-ray-dominated regions and can be used to search for pure AGNs, which is also supported by Imanishi et al. (2004, 2007). Imanishi et al. (2022) found significantly higher HCN-to-$\mathrm{HCO^+}$ $J = 2 \rightarrow 1$ flux ratios in a high fraction of some, but not all, AGN-important ULIRGs than that in starburst-classified sources. Some starburst-dominated galaxies may have HCN enhancement, which seems not to be driven by a single process. We include their flux ratios (Figure 5). The ALMA ULIRG sample (Imanishi et al. 2022) has an extreme contribution from AGNs, as discussed in the last paragraph of Section 5.5. In such conditions, the $\mathrm{HCN/HCO^+}$ line ratios might be enhanced by the chemistry from X-ray-dominated regions (Kohno et al. 2001; Harada et al. 2015).

The average HCN-to-$\mathrm{HCO^+}$ $J = 2 \rightarrow 1$ flux ratio in the Magellanic Clouds is 0.49 ± 0.34, which seems to be systematically lower than the ratios found in galaxies. This is consistent with Braine et al. (2017), who also found that $\mathrm{HCN/HCO^+}$ $J = 1 \rightarrow 0$ is lower in low-metallicity environments.

In both the Milky Way and external galaxies, the [N/O] abundance ratio has a positive correlation with [O/H] and [Fe/H] because nitrogen mostly originates from low-mass stars, and its nuclear production is a long-term process (Pilyugin et al. 2003; Liang et al. 2006). Therefore, the $\mathrm{HCN/HCO^+}$ abundance ratio would also decrease with [N/O] in low-metallicity environments such as the Magellanic Clouds, compared to normal metal-rich star-forming galaxies.

5.4. Influence of IR Pumping

Vibrational transitions of HCN and $\mathrm{HCO^+}$ are difficult to excite by collision, but they can be excited by absorbing IR photons at ~13–14 μm through IR pumping (Imanishi et al. 2017). Then the vibrational transitions can cascade to rotational transitions and enhance the HCN $J = 2 \rightarrow 1$ and/or $\mathrm{HCO^+}$ $J = 2 \rightarrow 1$ lines. If IR pumping becomes a dominant process, the dense gas mass estimated from HCN $J = 2 \rightarrow 1$ and/or $\mathrm{HCO^+}$ $J = 2 \rightarrow 1$ would be overestimated.

Sakamoto et al. (2010, 2021) found strong detections of HCN $v_2 = 1$ $J = 3 \rightarrow 2$, $J = 4 \rightarrow 3$ in NGC 4418 and Arp 220 by ALMA observations, indicating somewhat of an impact on the HCN rotational line. None of our spectra show any detections of HCN $v_2 = 1$ $J = 2 \rightarrow 1$, including NGC 4418 and Arp 220, possibly due to the limited signal-to-noise ratio of the APEX observation. Both NGC 4418 and Arp 220 show elevated $L'_{\mathrm{HCN}}/L'_{\mathrm{HCO^+}}$ ratios, especially among SF-dominated galaxies (see Figure 5), indicating the possible influence of IR pumping. The galaxies most heavily influenced by IR pumping in our sample are NGC 4418 and Arp 220. However, both NGC 4418 and Arp 220 show no outliers in correlations of L'_{dense}–L_{IR} and $\Sigma_{L'_{\mathrm{dense}}}$–$\Sigma_{L_{\mathrm{IR}}}$, indicating limited enhancement toward HCN $J = 2 \rightarrow 1$. Therefore, we do not expect a significant influence by IR pumping in our sample.

5.5. Comparison with Other HCN and $\mathrm{HCO^+}$ J = 2 → 1 Work

Imanishi et al. (2022) reported ALMA observations of HCN $J = 2 \rightarrow 1$ and $\mathrm{HCO^+}$ $J = 2 \rightarrow 1$ toward 10 ULIRGs, most of which contain AGNs. They also found positive correlations of L_{IR}–L'_{HCN} and L_{IR}–$L'_{\mathrm{HCO^+}}$.

We obtained the data (project codes: 2017.1.00022.S and 2017.1.00023.S) from the ALMA archive and processed the HCN and $\mathrm{HCO^+}$ $J = 2 \rightarrow 1$ data cubes with the standard pipeline. Overall, we got roughly consistent results compared to those in Imanishi et al. (2022). We then adopted the size estimated from the dust continuum given by Imanishi et al. (2022). Details of the measured fluxes and sizes are shown in Appendix D and Table 6.

In Figure 8, we overplot the ALMA ULIRG data on the HCN $J = 2 \rightarrow 1$ and $\mathrm{HCO^+}$ $J = 2 \rightarrow 1$ correlations. The ALMA ULIRG data seem to be systemically above both correlations of

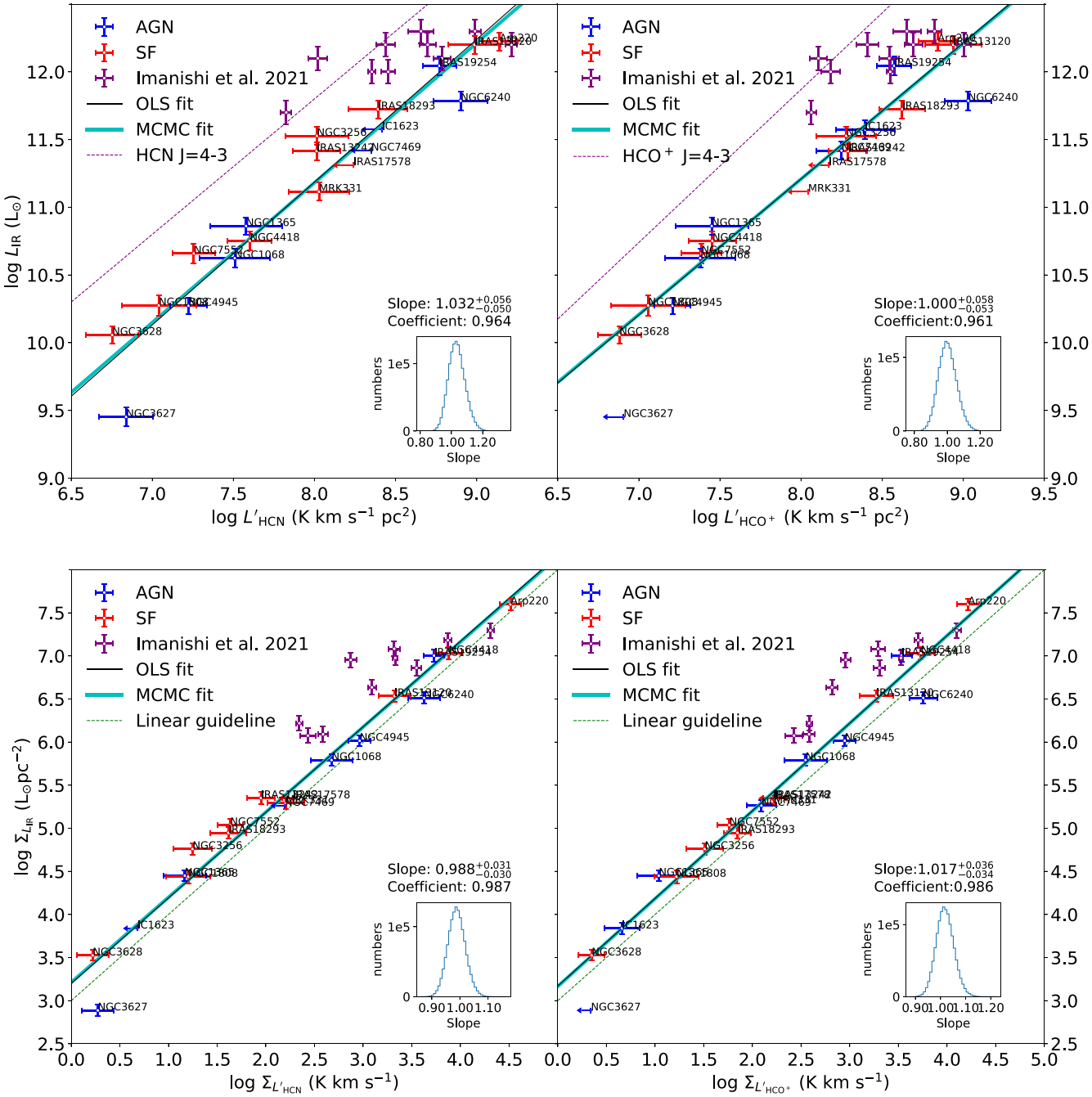

Figure 8. Correlations including the ALMA ULIRG sample from Imanishi et al. (2022). Top: correlations of $L'_{HCN} - L_{IR}$ (left) and $L'_{HCO^+} - L_{IR}$ (right). Bottom: correlations of $\Sigma_{L'_{HCN}} - \Sigma_{L_{IR}}$ (left) and $\Sigma_{L'_{HCO^+}} - \Sigma_{L_{IR}}$ (right). The AGN- and SF-dominated galaxies are shown in blue and red points, respectively. The fitting results of OLS and MCMC are shown in black and cyan lines, respectively. The green dashed line shows a linear relation for reference. The insets present the probability density distributions of the fitted slopes. Data points from Imanishi et al. (2022) are shown in purple and not included in the fitting. The purple dashed lines are the fitting results of HCN $J = 4 \rightarrow 3$ and HCO$^+$ $J = 4 \rightarrow 3$ obtained from Tan et al. (2018).

$L'_{\mathrm{denseJ=2\rightarrow1}}/L_{IR}$ and $\Sigma_{L'_{dense}} - \Sigma_{L_{IR}}$. For our APEX data, the orthogonal scatters on the correlation lines are 0.15 and 0.11 dex for HCN and HCO$^+$, respectively. And the mean orthogonal offsets of the ALMA ULIRG galaxies are 0.24 ± 0.22 and 0.27 ± 0.16 dex for HCN and HCO$^+$, respectively. Only two and one ALMA ULIRG galaxies lie in the 1σ range of our $L_{IR} - L'_{HCN}$ and $L_{IR} - L'_{HCO^+}$ correlations, respectively. Two and three galaxies of ALMA ULIRGs are off by $>3\sigma$ from the correlation lines of HCN and HCO$^+$, respectively.

This offset is consistent with that found by Imanishi et al. (2022), who found that the ALMA ULIRG $J = 2 \rightarrow 1$ data follow the $J = 4 \rightarrow 3$ relation given in Tan et al. (2018). Imanishi et al. (2022) interpreted that both HCN and HCO$^+$ are thermalized, which would make the HCN and HCO$^+$ $J = 4 \rightarrow 3$ line luminosities comparable to those of the $J = 2 \rightarrow 1$ transitions. From our APEX data, the fitted linear lines are systematically lower than those obtained from the $J = 4 \rightarrow 3$ data from Tan et al. (2018), making the ALMA ULIRGs above the $J = 2 \rightarrow 1$ relations.

Considering most of the ALMA ULIRGs are AGN-important ULIRGs, their L_{IR} might be dominated by AGNs, similar to the hot dust-obscured galaxies (hot-DOGs) found with WISE mid-IR

surveys (Wu et al. 2012; Tsai et al. 2015). The IR emission of hot-DOGs is mainly from the hot dust heated up by AGNs, which contribute, on average, >75% of the bolometric luminosity (Fan et al. 2016). On the other hand, the hot-DOGs also have high dust temperatures ($\langle T_{\rm dust}\rangle \sim 72$ K), which seems to be the same for the ALMA ULIRGs. The IRAS $f_{60\ \mu m}/f_{100\ \mu m}$ ratios of the ALMA ULIRGs are all higher than those of the APEX galaxies, except for NGC 4418, with average $f_{60\ \mu m}/f_{100\ \mu m}$ ratios of 1.09 ± 0.28 and 0.77 ± 0.19 for the ALMA ULIRGs and our APEX sample, respectively. Therefore, we suspect that the ALMA ULIRGs are AGN-dominated, IR-overluminous galaxies, and they should behave similarly for the $J = 1 \rightarrow 0$ lines of both HCN and HCO^+. The missing flux of the ALMA observation may also help to explain a few targets (for details, see Appendix D).

6. Summary

We present APEX observations toward HCN $J = 2 \rightarrow 1$ and HCO^+ $J = 2 \rightarrow 1$ in 17 nearby IR-bright star-forming galaxies. Combining HCN $J = 2 \rightarrow 1$ and HCO^+ $J = 2 \rightarrow 1$ data in the literature, and with the total IR luminosity fitted from the dust SED, we correlate slopes of 1.03 ± 0.05 and 1.00 ± 0.05 for $L'_{\rm HCO^+} - L_{\rm IR}$ and $L'_{\rm HCN} - L_{\rm IR}$, respectively.

To obtain correlations of surface densities, which could eliminate the biases from uncertain distances, we use the size of the 1.4 GHz radio continuum to normalize the luminosities of both IR emission ($\Sigma_{L_{\rm IR}}$) and dense gas tracers ($\Sigma_{L'_{\rm HCN}}$ and $\Sigma_{L'_{\rm HCO^+}}$). These surface density correlations also show linear slopes of 0.99 ± 0.03 and 1.02 ± 0.03 for the HCN and HCO^+ $J = 2 \rightarrow 1$ lines, respectively. The slope errors and p-values of the surface density correlations are also smaller than those of the luminosity correlations. The Spearman correlation coefficients of the $J = 2 - 1$ lines (0.98 and 0.96 for HCN $J = 2 \rightarrow 1$ and HCO^+ $J = 2 \rightarrow 1$) are higher than those obtained from the $J = 1 - 0$ (0.94 for HCN $J = 1 \rightarrow 0$; Gao & Solomon 2004a) and the $J = 4 - 3$ (0.89 and 0.84 for HCN $J = 4 \rightarrow 3$ and HCO^+ $J = 4 \rightarrow 3$; Tan et al. 2018) transitions, indicating the advantage of the $J = 2 \rightarrow 1$ transitions of HCN and HCO^+ in tracing the star-forming gas.

Comparing with the HCN $J = 2 \rightarrow 1$ and HCO^+ $J = 2 \rightarrow 1$ data from star-forming clouds of the Magellanic Clouds (Galametz et al. 2020), we find that the low-metallicity environment not only slightly deviates the data from the overall surface density correlations but also biases the HCN $J = 2 \rightarrow 1$/HCO^+ $J = 2 \rightarrow 1$ line ratio to low ratios. This is consistent with previous findings in low-metallicity galaxies (e.g., Braine et al. 2017). The systematically lower HCN/HCO^+ ratios are possibly due to the variation of the [N/O] elemental abundance variation in low-metallicity environments.

On the other hand, when comparing with the ULIRG sample from Imanishi et al. (2022), those AGN-important galaxies lie systematically above both correlations of $L'_{\rm dense}$–$L_{\rm IR}$ and $\Sigma_{L'_{\rm dense}}$–$\Sigma_{L_{\rm IR}}$ found in our APEX sample. This is likely due to the AGN contribution to the total IR luminosity for such compact objects, which could heavily overestimate SFRs. Therefore, the contribution from AGNs may not be negligible in such extreme conditions.

We thank Dr. Maud Galametz for providing the HCN and HCO^+ data of the Magellanic Clouds in Galametz et al. (2020). Z.Y.Z. and J.Z. acknowledge the support of the National Natural Science Foundation of China (NSFC) under grant Nos. 12041305 and 12173016, the Program for Innovative Talents, Entrepreneur in Jiangsu, and the science research grants from the China Manned Space Project with Nos. CMS-CSST-2021-A08 and CMS-CSST-2021-A07. C.Y. acknowledges support from ERC Advanced Grant 789410. This publication is based on data acquired with the Atacama Pathfinder Experiment (APEX). APEX is a collaboration between the Max-Planck-Institut fur Radioastronomie, the European Southern Observatory, and the Onsala Space Observatory. Herschel was an ESA space observatory with science instruments provided by European-led Principal Investigator consortia and important participation from NASA. PACS has been developed by a consortium of institutes led by MPE (Germany) and including UVIE (Austria); KU Leuven, CSL, and IMEC (Belgium); CEA and LAM (France); MPIA (Germany); INAFIFSI/OAA/OAP/OAT, LENS, and SISSA (Italy); and IAC (Spain). This development has been supported by the funding agencies BMVIT (Austria), ESA-PRODEX (Belgium), CEA/CNES (France), DLR (Germany), ASI/INAF (Italy), and CICYT/MCYT (Spain). SPIRE has been developed by a consortium of institutes led by Cardiff University (UK) and including the University of Lethbridge (Canada); NAOC (China); CEA and LAM (France); IFSI and the University of Padua (Italy); IAC (Spain); Stockholm Observatory (Sweden); Imperial College London, RAL, UCL-MSSL, UKATC, and Univ. Sussex (UK); and Caltech, JPL, NHSC, and the University of Colorado (USA). This development has been supported by national funding agencies: CSA (Canada); NAOC (China); CEA, CNES, and CNRS (France); ASI (Italy); MCINN (Spain); SNSB (Sweden); STFC and UKSA (UK); and NASA (USA). This work is based in part on observations made with the Spitzer Space Telescope, which was operated by the Jet Propulsion Laboratory, California Institute of Technology, under a contract with NASA. This publication makes use of data products from the Wide-field Infrared Survey Explorer, which is a joint project of the University of California, Los Angeles, and the Jet Propulsion Laboratory/California Institute of Technology, funded by the National Aeronautics and Space Administration. This paper makes use of the following ALMA data: ADS/JAO.ALMA#2015.1.00717.S. ALMA is a partnership of ESO (representing its member states), NSF (USA), and NINS (Japan), together with NRC (Canada) and NSC and ASIAA (Taiwan) and KASI (Republic of Korea), in cooperation with the Republic of Chile. The Joint ALMA Observatory is operated by ESO, AUI/NRAO and NAOJ.

Software: GILDAS/CLASS (Pety 2005), Numpy (van der Walt et al. 2011; Harris et al. 2020), emcee (Foreman-Mackey et al. 2013), Photutils (Bradley et al. 2019).

Appendix A
Background Subtraction

When measuring the IR flux of each galaxy, we need to subtract the background to avoid possible contamination from other nearby sources and compute the error from the rms error of the IR image. First, we remove strong sources higher than 3σ using the python package PHOTUTILS.[12] Then we take the initial flat-field subtraction using the average flux of the selected background area. We compute the total flux in a small circle and increase the radius of the circle until the flux in the circle does not increase. To show the size that can cover the total flux of the galaxy, we plot the flux varying with the

[12] https://pypi.org/project/photutils/0.4/

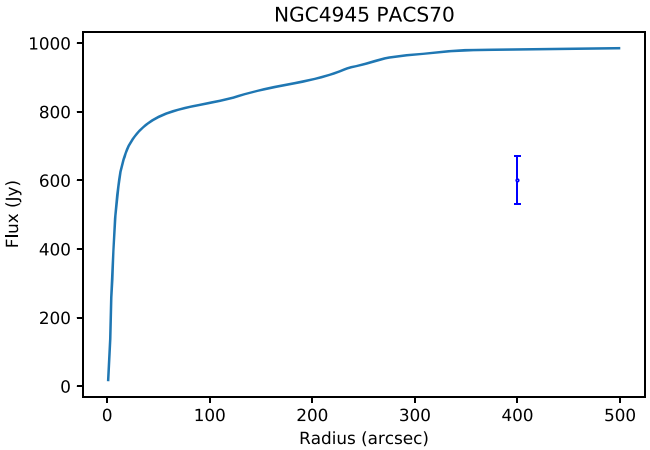

Figure 9. Example of the curve of flux growth of the PACS 70 μm map of NGC 4945. *Y*-axis is flux within the circle of a certain radius. The error bar shows background rms plus 7% absolute flux calibration error.

circle's radius in Figure 9. Finally, we choose the annulus within 1.0× and 1.5× this radius as the background.

Appendix B
Two-component Dust SED Fitting

We download 11 bands of IR data observed by Spitzer and Herschel from 3.4 to 500 μm. We convolve them to the same resolution and then do the photometry. We try SED fitting with different bands of data, and we find that short-wavelength bands ($<$12 μm) could suffer from contamination of stars or PAH emission, and they are higher than that predicted by the MBB models. We also use IRAS low-resolution ($\sim$4′) flux for comparison; for most cases, it includes the total fluxes of the whole galaxies. We compute the scaling factor from MIPS 24 μm and PACS 70 μm data. We include the 60 μm and exclude the 25 μm data points. One example of dust SED fitting is shown in Figure 10.

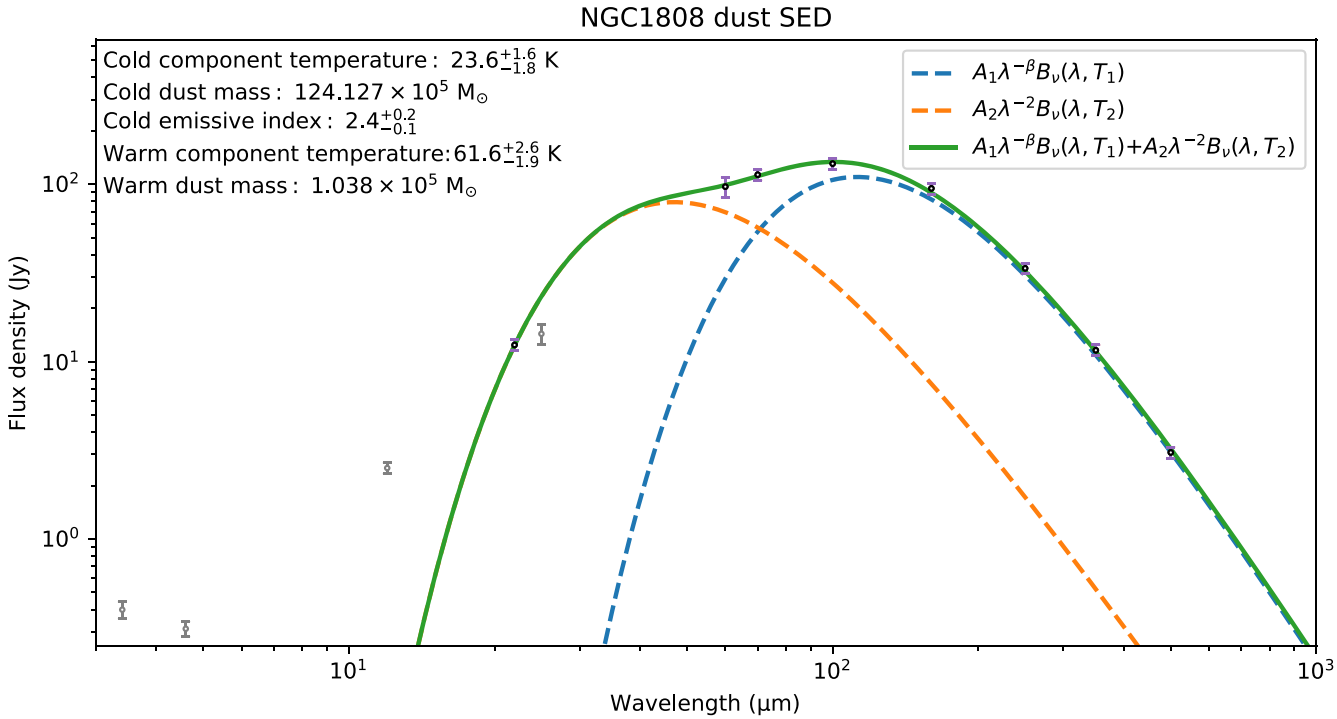

Figure 10. Example of the dust SED of NGC 1808. The orange and blue dashed lines represent the warm and cold components, respectively. The gray data points represent bands not in the fitting, including WISE 3.4, 4.6, and 12 μm and IRAS 25 μm, due to short wavelength or low resolution.

Appendix C
Different IR Bands as SFR Tracers

To infer an IR band that could better trace SFR, we compare total IR (3–1000 μm), far-IR (100–1000 μm), near-/mid-IR (3–100 μm), and warm component luminosity versus dense gas luminosity. We fit the relationship with the MCMC and least-squares methods to get the slope and compute the coefficient with the python package NUMPY. We show the comparison plots in Figure 11. We find that the near-/mid-IR contributes most of the total IR luminosity and is ∼three times higher than the far-IR luminosity. However, the far-IR luminosity is a little more stable than near-/mid-IR according to their slopes using different SED fitting methods with different IR bands. We finally choose the total IR luminosity to trace SFR.

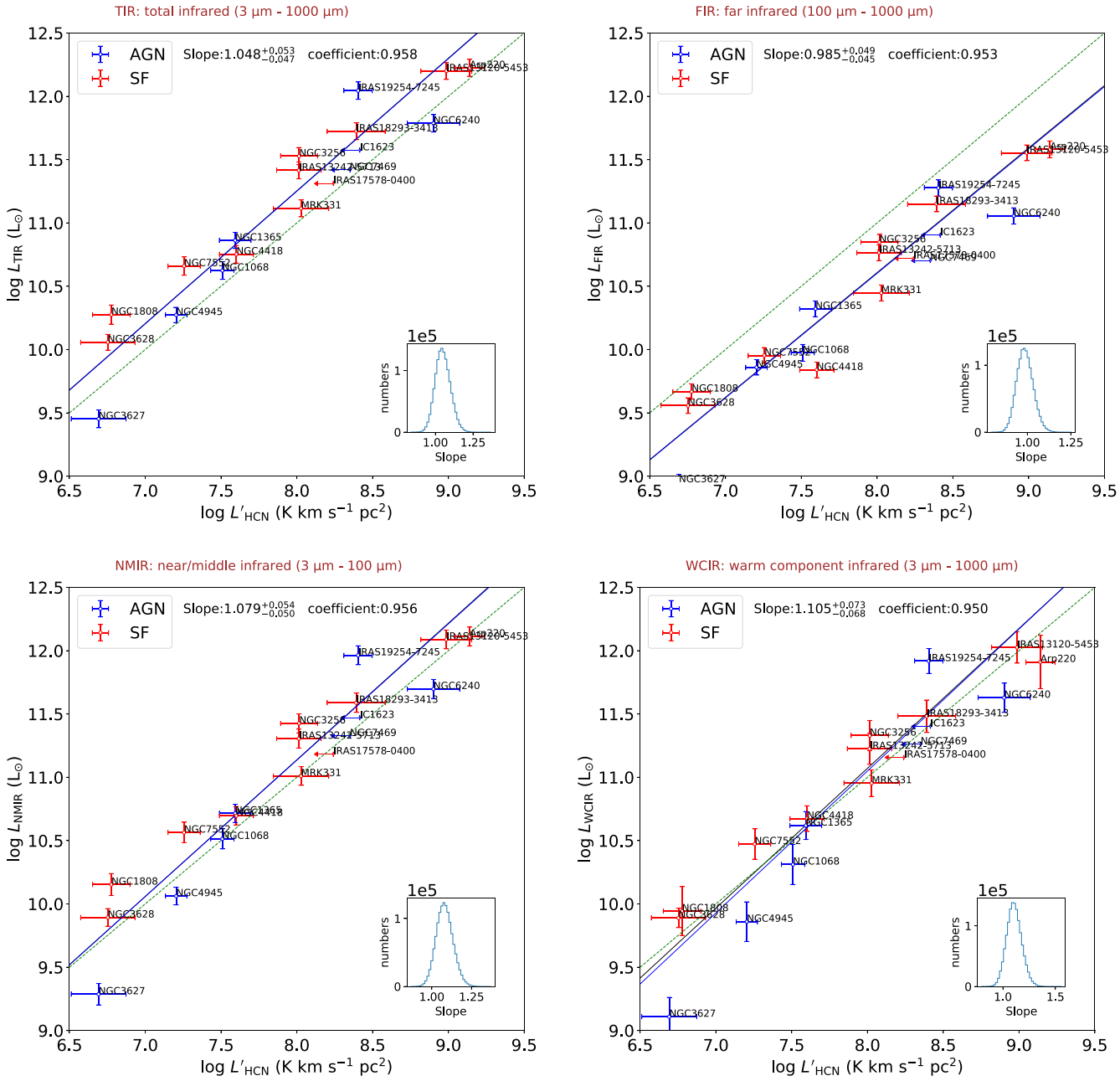

Figure 11. Correlations between L'_{HCN} and luminosities of different IR bands. Top left: total IR luminosity. Top right: far-IR luminosity. Bottom left: near-/mid-IR luminosity. Bottom right: warm component IR luminosity. The adopted wavelength ranges and dust components are labeled at the top of each panel.

Appendix D
Remeasure ALMA HCN and HCO^+ $J = 2 \rightarrow 1$ Flux

We reprocessed the HCN and HCO^+ $J = 2 \rightarrow 1$ data reported in Imanishi et al. (2022). For IRAS 12127–1412, IRAS 13509+0442, and Superantennae, there are no available HCN and HCO^+ $J = 2 \rightarrow 1$ imaging products. So we downloaded their data, reprocessed with the pipeline, and reimaged with robust = 1.5 with task TCLEAN. For others, we adopted the delivered data products. We remeasured the line fluxes of HCN and HCO^+ $J = 2 \rightarrow 1$ in all targets with the aperture size determined by the curve of flux growth (described in Appendix A) of the moment zero map of the initial estimated HCN and HCO^+. The remeasured line fluxes are shown in Table 6. The fluxes of NGC 1614, IRAS 13509+0442, and IRAS 22491–1808 are significantly higher than those reported in Imanishi et al. (2022; >80%), and the fluxes of three other galaxies are ∼30% higher.

The missing flux of large-scale structures during the interferometric observations may also play a role in biasing the sample distributions, along with the AGN bolometric contribution. For example, NGC 1614 has been observed with CO $J = 1 \rightarrow 0$ and ^{13}CO $J = 1 \rightarrow 0$ (König et al. 2016), which show a gaseous disk of ∼10″–15″ in diameter. The ALMA HCN $J = 2 \rightarrow 1$ observations only revealed the central emitting region of ∼2″–3″ in diameter, which may indicate potentially extended fluxes filtered by ALMA. While IRAS 12112+0305 has been resolved into two nuclei, Evans et al. (2002) imaged its CO distribution and showed extended emission around the nuclei.

ALMA's shortest baseline is ∼15 m, corresponding to the largest scale of 30″. However, in the *uv* data of IRAS 12127–1412, IRAS 13509+0442, and Superantennae, most short baselines are flagged, possibly due to antenna shadowing. Thus, the largest recovered scale is 12″, similar to the scales of NGC 1614 and IRAS 12112+0305. However, it is difficult to evaluate how much the missing flux would be without single-dish observations.

Appendix E
Dust Temperature in AGN-host and SF-dominated Galaxies

The IR luminosity of ULIRGs in Imanishi et al. (2022) may be enhanced by AGN-heated hot dust (Section 5.5). Here we check whether the dust temperatures of the galaxies in our sample are influenced by AGN activities by plotting dust temperature versus IR luminosity surface density in different galaxy types (see Figure 12). Dust temperatures are obtained under the assumption of an MBB with a fixed warm component emissivity index of 2. Figure 12 shows the results of the IR luminosity surface density and the cold dust temperature fitted with these assumptions in the left panel. The right panel of Figure 12 shows IR luminosity surface density versus warm dust temperature. The caption mentions that T_c and T_w are the cold and warm dust temperature, respectively. There is no significant relation between dust temperature and galaxy type or $\Sigma_{L_{IR}}$.

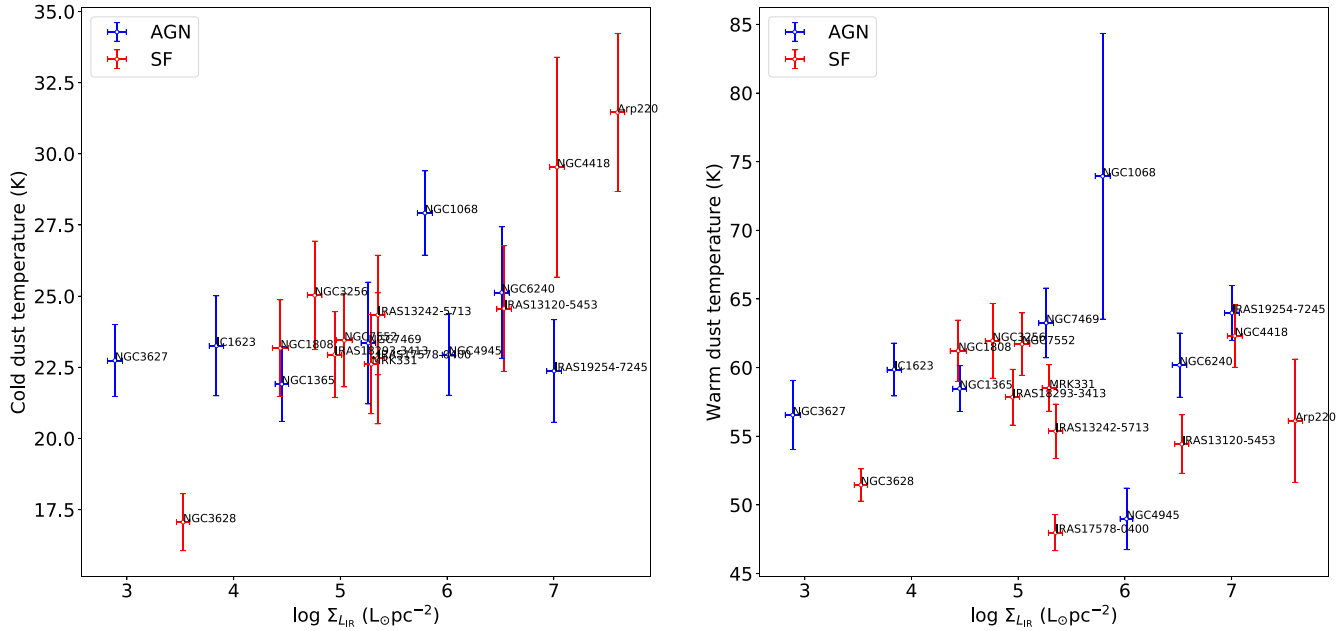

Figure 12. (Left) Cold dust temperature (T_c) as a function of IR luminosity surface density ($\Sigma_{L_{IR}}$). (Right) Warm dust temperature (T_w) as a function of $\Sigma_{L_{IR}}$. The AGN- and SF-dominated galaxies are shown in blue and red points, respectively.

ORCID iDs

Jing Zhou https://orcid.org/0000-0002-0818-1745
Zhi-Yu Zhang https://orcid.org/0000-0002-7299-2876
Yu Gao https://orcid.org/0000-0003-0007-2197
Junzhi Wang https://orcid.org/0000-0001-6106-1171
Yong Shi https://orcid.org/0000-0002-8614-6275
Qiusheng Gu https://orcid.org/0000-0002-3890-3729
Chentao Yang https://orcid.org/0000-0002-8117-9991
Tao Wang https://orcid.org/0000-0002-2504-2421
Qing-Hua Tan https://orcid.org/0000-0003-3032-0948

References

Aniano, G., Draine, B. T., Gordon, K. D., & Sandstrom, K. 2011, PASP, 123, 1218
Baan, W. A., Henkel, C., Loenen, A. F., Baudry, A., & Wiklind, T. 2008, A&A, 477, 747
Balog, Z., Müller, T., Nielbock, M., et al. 2014, ExA, 37, 129
Belitsky, V., Lapkin, I., Fredrixon, M., et al. 2018, A&A, 612, A23
Bell, E. F. 2003, ApJ, 586, 794
Bigiel, F., Leroy, A., Walter, F., et al. 2008, AJ, 136, 2846
Bolatto, A. D., Wolfire, M., & Leroy, A. K. 2013, ARA&A, 51, 207
Bradley, L., Sipocz, B., Robitaille, T., et al. 2019, astropy/photutils: v0.6, Zenodo, doi:10.5281/zenodo.2533376
Braine, J., Shimajiri, Y., André, P., et al. 2017, A&A, 597, A44
Cicone, C., Severgnini, P., Papadopoulos, P. P., et al. 2018, ApJ, 863, 143
Cole, G. H. J., Mundell, C. G., & Pedlar, A. 1998, MNRAS, 300, 656
Condon, J. J. 1987, ApJS, 65, 485
Condon, J. J., Cotton, W. D., Jarrett, T., et al. 2021, ApJS, 257, 35
Condon, J. J., & Ransom, S. M. 2016, Essential Radio Astronomy (Princeton, NJ: Princeton Univ. Press)
Costagliola, F., Aalto, S., Sakamoto, K., et al. 2013, A&A, 556, A66
de Vaucouleurs, G., de Vaucouleurs, A., Corwin, H. G. J., et al. 1991, Third Reference Catalogue of Bright Galaxies (New York, NY: Springer)
Deller, A. T., & Middelberg, E. 2014, AJ, 147, 14
Evans, A. S., Mazzarella, J. M., Surace, J. A., & Sanders, D. B. 2002, ApJ, 580, 749
Evans, N. J. I., Kim, K.-T., Wu, J., et al. 2020, ApJ, 894, 103
Fan, L., Han, Y., Nikutta, R., Drouart, G., & Knudsen, K. K. 2016, ApJ, 823, 107
Fixsen, D. J., Cheng, E. S., Gales, J. M., et al. 1996, ApJ, 473, 576
Foreman-Mackey, D., Hogg, D. W., Lang, D., & Goodman, J. 2013, PASP, 125, 306
Galametz, M., Kennicutt, R. C., Calzetti, D., et al. 2013, MNRAS, 431, 1956
Galametz, M., Schruba, A., De Breuck, C., et al. 2020, A&A, 643, A63
Galametz, M., Zhang, Z. Y., Immer, K., et al. 2016, MNRAS Lett., 462, L36
Gallimore, J. F., & Beswick, R. 2004, AJ, 127, 239
Gao, Y., & Solomon, P. M. 2004a, ApJ, 606, 271
Gao, Y., & Solomon, P. M. 2004b, ApJS, 152, 63
García-Burillo, S., Graciá-Carpio, J., Guélin, M., et al. 2006, ApJL, 645, L17
Greve, T. R., Papadopoulos, P. P., Gao, Y., & Radford, S. J. E. 2009, ApJ, 692, 1432
Griffin, M. J., Abergel, A., Abreu, A., et al. 2010, A&A, 518, L3
Harada, N., Riquelme, D., Viti, S., et al. 2015, A&A, 584, A102
Harris, C. R., Millman, K. J., van der Walt, S. J., et al. 2020, Natur, 585, 357
Hayward, C. C., Lanz, L., Ashby, M. L. N., et al. 2014, MNRAS, 445, 1598
Heiderman, A., Evans, N. J. I., Allen, L. E., Huard, T., & Heyer, M. 2010, ApJ, 723, 1019
Herrero-Illana, R., Pérez-Torres, M. Á, Randriamanakoto, Z., et al. 2017, MNRAS, 471, 1634
Imanishi, M., Nakanishi, K., & Izumi, T. 2016, AJ, 152, 218
Imanishi, M., Nakanishi, K., & Izumi, T. 2017, ApJ, 849, 29
Imanishi, M., Nakanishi, K., Izumi, T., & Baba, S. 2022, ApJ, 926, 159
Imanishi, M., Nakanishi, K., Kuno, N., & Kohno, K. 2004, AJ, 128, 2037
Imanishi, M., Nakanishi, K., Tamura, Y., Oi, N., & Kohno, K. 2007, AJ, 134, 2366
Immer, K., Belitsky, V., Olberg, M., et al. 2016, Msngr, 165, 13
Iono, D., Wilson, C. D., Takakuwa, S., et al. 2007, ApJ, 659, 283
Jang, I. S., & Lee, M. G. 2017, ApJ, 836, 74
Jeřábková, T., Kroupa, P., Dabringhausen, J., Hilker, M., & Bekki, K. 2017, A&A, 608, A53
Juneau, S., Narayanan, D. T., Moustakas, J., et al. 2009, ApJ, 707, 1217
Karachentsev, I. D., & Makarov, D. A. 1996, AJ, 111, 794
Kennicutt, R. C., & Evans, N. J. 2012, ARA&A, 50, 531
Kennicutt, R. C. J. 1998a, ARA&A, 36, 189
Kennicutt, R. C. J. 1998b, ApJ, 498, 541
Knudsen, K. K., Walter, F., Weiss, A., et al. 2007, ApJ, 666, 156
Kohno, K., Matsushita, S., Vila-Vilaró, B., et al. 2001, in ASP Conf. Proc. 249, The Central Kiloparsec of Starbursts and AGN: The La Palma Connection (San Francisco, CA: ASP), 672
Kollatschny, W., Weilbacher, P. M., Ochmann, M. W., et al. 2020, A&A, 633, A79
König, S., Aalto, S., Muller, S., et al. 2016, A&A, 594, A70
Koshida, S., Yoshii, Y., Kobayashi, Y., et al. 2017, ApJL, 842, L13
Krips, M., Neri, R., García-Burillo, S., et al. 2008, ApJ, 677, 262
Kroupa, P. 2001, MNRAS, 322, 231
Lenc, E., & Tingay, S. J. 2009, AJ, 137, 537
Li, A., & Draine, B. T. 2001, ApJ, 554, 778
Li, F., Wang, J., Fang, M., et al. 2020a, MNRAS, 494, 1095
Li, F., Wang, J., Fang, M., et al. 2020b, PASJ, 72, 41
Liang, Y. C., Yin, S. Y., Hammer, F., et al. 2006, ApJ, 652, 257
Lintott, C., & Viti, S. 2006, ApJL, 646, L37
Liu, L., Gao, Y., & Greve, T. R. 2015, ApJ, 805, 31
Lonsdale, C. J., Lonsdale, C. J., Smith, H. E., & Diamond, P. J. 2003, ApJ, 592, 804
Lu, N., Zhao, Y., Xu, C. K., et al. 2015, ApJL, 802, L11
McMullin, J. P., Waters, B., Schiebel, D., Young, W., & Golap, K. 2007, in ASP Conf. Ser. 376, Astronomical Data Analysis Software and Systems XVI, ed. R. A. Shaw, F. Hill, & D. J. Bell (San Francisco, CA: ASP), 127
Meijerink, R., Kristensen, L. E., Weiß, A., et al. 2013, ApJL, 762, L16
Mould, J. R., Huchra, J. P., Freedman, W. L., et al. 2000, ApJ, 529, 786
Muller, E., Ott, J., Hughes, A., et al. 2010, ApJ, 712, 1248
Murphy, E. J., Condon, J. J., Schinnerer, E., et al. 2011, ApJ, 737, 67
Murphy, E. J., Dong, D., Leroy, A. K., et al. 2015, ApJ, 813, 118
Nasonova, O. G., de Freitas Pacheco, J. A., & Karachentsev, I. D. 2011, A&A, 532, A104
Neugebauer, G., Habing, H. J., van Duinen, R., et al. 1984, ApJL, 278, L1
Nguyen, Q. R., Jackson, J. M., Henkel, C., Truong, B., & Mauersberger, R. 1992, ApJ, 399, 521
Padovani, P., Alexander, D. M., Assef, R. J., et al. 2017, A&ARv, 25, 2
Papadopoulos, P. P. 2007, ApJ, 656, 792
Papadopoulos, P. P., van der Werf, P. P., Xilouris, E. M., et al. 2012, MNRAS, 426, 2601
Papadopoulos, P. P., Zhang, Z.-Y., Xilouris, E. M., et al. 2014, ApJ, 788, 153
Pety, J. 2005, in EdP-Sciences, Conf. Ser., SF2A-2005, 1, ed. F. Casoli (Paris: EdP-Science), 721
Pilbratt, G. L., Riedinger, J. R., Passvogel, T., et al. 2010, A&A, 518, L1
Pilyugin, L. S., Thuan, T. X., & Vílchez, J. M. 2003, A&A, 397, 487
Poglitsch, A., Waelkens, C., Geis, N., et al. 2010, A&A, 518, L2
Privon, G. C., Herrero-Illana, R., Evans, A. S., et al. 2015, ApJ, 814, 39
Radford, S. J. E., Delannoy, J., Downes, D., et al. 1991, in IAU Symp. 146, Dynamics of Galaxies and Their Molecular Cloud Distributions, ed. F. Combes & F. Casoli (Dordrecht: Kluwer), 303
Rieke, G. H., Young, E. T., Engelbracht, C. W., et al. 2004, ApJS, 154, 25
Roy, A. L., Colbert, E. J. M., Wilson, A. S., & Ulvestad, J. S. 1998, ApJ, 504, 147
Russell, D. G. 2002, ApJ, 565, 681
Saikia, D. J., Unger, S. W., Pedlar, A., et al. 1990, MNRAS, 245, 397
Sakamoto, K., Aalto, S., Evans, A. S., Wiedner, M. C., & Wilner, D. J. 2010, ApJL, 725, L228
Sakamoto, K., Martín, S., Wilner, D. J., et al. 2021, ApJ, 923, 240
Sanders, D. B., Mazzarella, J. M., Kim, D. C., Surace, J. A., & Soifer, B. T. 2003, AJ, 126, 1607
Sandqvist, A., Joersaeter, S., & Lindblad, P. O. 1995, A&A, 295, 585
Schöier, F. L., van der Tak, F. F. S., van Dishoeck, E. F., & Black, J. H. 2005, A&A, 432, 369
Shirley, Y. L. 2015, PASP, 127, 299
Sliwa, K., Wilson, C. D., Aalto, S., & Privon, G. C. 2017, ApJL, 840, L11
Smith, H. E., Lonsdale, C. J., & Lonsdale, C. J. 1998, ApJ, 492, 137
Solomon, P. M., Downes, D., & Radford, S. J. E. 1992, ApJL, 387, L55
Solomon, P. M., & Vanden Bout, P. A. 2005, ARA&A, 43, 677
Spergel, D. N., Bean, R., Doré, O., et al. 2007, ApJS, 170, 377
Tacconi, L. J., Genzel, R., Tecza, M., et al. 1999, ApJ, 524, 732
Tan, Q.-H., Gao, Y., Zhang, Z.-Y., et al. 2018, ApJ, 860, 165
Theureau, G., Hanski, M. O., Coudreau, N., Hallet, N., & Martin, J. M. 2007, A&A, 465, 71
Tsai, C.-W., Eisenhardt, P. R. M., Wu, J., et al. 2015, ApJ, 805, 90
Tully, R. B., Courtois, H. M., Dolphin, A. E., et al. 2013, AJ, 146, 86

Tully, R. B., & Fisher, J. R. 1988, Catalog of Nearby Galaxies (Cambridge: Cambridge Univ. Press)
Tully, R. B., Libeskind, N. I., Karachentsev, I. D., et al. 2015, ApJL, 802, L25
U, V., Sanders, D. B., Mazzarella, J. M., et al. 2012, ApJS, 203, 9
van der Walt, S., Colbert, S. C., & Varoquaux, G. 2011, CSE, 13, 22
Varenius, E., Conway, J. E., Martí-Vidal, I., et al. 2014, A&A, 566, A15
Varenius, E., Conway, J. E., Martí-Vidal, I., et al. 2016, A&A, 593, A86
Wang, M., Henkel, C., Chin, Y. N., et al. 2004, A&A, 422, 883
Werner, M. W., Roellig, T. L., Low, F. J., et al. 2004, ApJS, 154, 1
White, R. L. 1985, ApJ, 289, 698
Willick, J. A., & Batra, P. 2001, ApJ, 548, 564
Wong, T., Hughes, A., Ott, J., et al. 2011, ApJS, 197, 16
Wu, J., Evans, N. J. I., Gao, Y., et al. 2005, ApJL, 635, L173
Wu, J., Evans, N. J. I., Shirley, Y. L., & Knez, C. 2010, ApJS, 188, 313
Wu, J., Tsai, C.-W., Sayers, J., et al. 2012, ApJ, 756, 96
Zhang, Z.-Y., Gao, Y., Henkel, C., et al. 2014, ApJL, 784, L31
Zhang, Z.-Y., Romano, D., Ivison, R. J., Papadopoulos, P. P., & Matteucci, F. 2018, Natur, 558, 260
Zhu, Y.-N., Wu, H., Cao, C., & Li, H.-N. 2008, ApJ, 686, 155